

## Improving the twilight model for polar cap absorption nowcasts

N. C. Rogers<sup>1</sup>, A. Kero<sup>2</sup>, F. Honary<sup>1</sup>, P. T. Verronen<sup>3</sup>, E. M. Warrington<sup>4</sup>,  
and D. W. Danskin<sup>5</sup>

<sup>1</sup> Department of Physics, Lancaster University, UK.

<sup>2</sup> Sodankylä Geophysical Observatory, University of Oulu, Sodankylä, Finland.

<sup>3</sup> Earth Observation Unit, Finnish Meteorological Institute, Helsinki, Finland.

<sup>4</sup> Department of Engineering, University of Leicester, UK.

<sup>5</sup> Geomagnetic Laboratory, Natural Resources Canada, Ottawa, Ontario, Canada.

Corresponding author: Neil Rogers ([n.rogers1@lancaster.ac.uk](mailto:n.rogers1@lancaster.ac.uk))

### Key Points:

- Parameters of an empirical PCA model are optimized using riometers
- A linear twilight transition model provides a better fit than ‘Earth-shadow’ methods
- Post-sunrise delays in absorption increases are large and highly variable

This article has been accepted for publication and undergone full peer review but has not been through the copyediting, typesetting, pagination and proofreading process which may lead to differences between this version and the Version of Record. Please cite this article as doi: 10.1002/2016SW001527

## Abstract

During Solar Proton Events (SPE), energetic protons ionize the polar mesosphere causing HF radiowave attenuation, more strongly on the dayside where the effective recombination coefficient,  $\alpha_{eff}$ , is low. Polar cap absorption (PCA) models predict the 30 MHz cosmic noise absorption,  $A$ , measured by riometers, based on real-time measurements of the integrated proton flux-energy spectrum,  $J$ . However, empirical models in common use cannot account for regional and day-to-day variations in the day- and nighttime profiles of  $\alpha_{eff}(z)$  or the related sensitivity parameter,  $m = A/\sqrt{J}$ . Large prediction errors occur during twilight when  $m$  changes rapidly, and due to errors locating the rigidity cutoff latitude. Modeling the twilight change in  $m$  as a linear or Gauss error-function transition over a range of solar-zenith angles ( $\chi_l < \chi < \chi_u$ ) provides a better fit to measurements than selecting day or night  $\alpha_{eff}$  profiles based on the Earth-shadow height. Optimal model parameters were determined for several polar cap riometers for large SPEs in 1998-2005. The optimal  $\chi_l$  parameter was found to be most variable, with smaller values (as low as  $60^\circ$ ) post-sunrise compared with pre-sunset, and with positive correlation between riometers over a wide area. Day and night values of  $m$  exhibited higher correlation for closely spaced riometers. A nowcast simulation is presented in which rigidity boundary latitude and twilight model parameters are optimized by assimilating age-weighted measurements from 25 riometers. The technique reduces model bias, and root-mean-squared errors are reduced by up to 30% compared with a model employing no riometer data assimilation.

## 1 Introduction

High-Frequency (HF) (3-30MHz) radio signals propagated via the high-latitude ionosphere are occasionally subject to intense Polar Cap Absorption (PCA) [Bailey, 1964]. The signal attenuation arises from an increased ionisation of the D-region ionosphere caused by energetic protons precipitating during Solar Proton Events (SPE) [Shea and Smart, 1990; Kurt et al., 2004]. SPEs follow intense Earth-directed solar flares and interplanetary coronal mass ejections, and are defined by a flux of  $> 10$  MeV protons,  $J(> 10 \text{ MeV})$  in the near-Earth environment exceeding 10 particle flux units ( $1 \text{ pfu} = 1 \text{ cm}^{-2} \text{ sr}^{-1} \text{ s}^{-1}$ ).

For decades, riometers have been used to measure cosmic noise absorption (CNA) at approximately 30 MHz [Little and Leinbach, 1959; Friedrich et al., 2002; Rostoker et al., 1995; Honary et al., 2011; Browne et al., 1995]. Riometers continuously measure cosmic radio noise and ionospheric absorption is determined from the difference with a ‘quiet day curve’ (QDC), which is the expected diurnal variation of noise in the absence of absorption [CANOPUS, 2005]. The largest SPEs result in several decibels of CNA and may persist for several days. At lower latitudes the geomagnetic field shields charged particles with less than a threshold ‘rigidity’,  $R_c$ , (momentum per unit charge) and so the CNA is much reduced at these latitudes.

Riometers are operational at over 60 locations worldwide (see <http://spears.lancs.ac.uk/cgi-bin/riometers>) and many of these now have the capability to stream data online in real-time (<15 minutes latency) [Danskin et al., 2008]. Figure 1 maps the locations of riometers currently operated by four institutions: The University of Calgary, Canada – which operates the Northern Solar Terrestrial Array (NORSTAR) [Rostoker et al., 1995]; Natural Resources Canada (NRCan) [Danskin et al., 2008]; the Sodankylä Geophysical Observatory (SGO); and Lancaster University, UK, which operates an imaging riometer at Kilpisjärvi, Finland.

Locations and operating frequencies of each riometer are listed in Table 1. The aim of current

research is to incorporate real-time riometer measurements into HF radio propagation nowcasts (i.e. absorption predictions up to a few hours ahead) which would be of particular value to HF radio services operating in polar regions, such as air-traffic communications [Warrington *et al.*, 2016a, 2016b; Neal *et al.*, 2013].

PCA models relate CNA to measurements of the flux of energetic solar protons, measured by the Space Environment Monitor (SEM) on-board the Geostationary Operational Environment Satellites (GOES). These are published online with less than 5-minutes latency by the US National Oceanic and Atmospheric Administration (NOAA) (<http://www.swpc.noaa.gov/products/goes-proton-flux>) and may be forecast hours or days ahead [Núñez, 2011; Ji *et al.*, 2014]. Estimates of current and forecast geomagnetic indices  $K_p$  and  $D_{st}$  required for models of the rigidity cutoff latitude [Smart *et al.*, 1999; Nesse Tyssøy and Stadsnes, 2015; Dmitriev *et al.*, 2010] may also be derived from real-time measurements of the solar wind and interplanetary magnetic field from spacecraft near the  $L_1$  Sun-Earth Lagrange point [Wing *et al.*, 2005; Temerin and Li, 2002, 2006].

The chemical and ionic composition and the temperature of the ionospheric D-region varies both regionally and over time, particularly during the course of an SPE [Ondrášková *et al.*, 2003, 2008; Ondrášková and Krivolutsky, 2005; Osepian *et al.*, 2008, 2009]. This means that PCA models incorporating only the x-ray flux, particle flux and solar wind data in real-time will not be optimal for all locations at all times. Riometers provide an indirect measurement of this variable ionospheric response and Rogers and Honary [2015] demonstrated how parameters of PCA models could be optimized on a real-time basis by regression to age-weighted riometer measurements. This resulted in reductions in the root-mean-squared error (RMSE) of typically 20-40%. Future work will demonstrate how these real-time updated

absorption models can be used to improve HF signal strength predictions employing a ray-tracing model for a high-latitude propagation path.

This paper compares riometer measurements with predictions of

1. Two physics-based ‘full profile’ PCA models (the ‘Type 2’ model of *Rogers and Honary* [2015] and the Sodankylä Ionospheric Chemistry model [*Verronen et al.*, 2005]), which incorporate altitude profiles of atmospheric neutral densities and temperatures;
2. An empirical PCA model that does not require altitude profiles, and which is based on the strong correlation between CNA and the square-root of the flux of energetic solar protons.

Large errors in model prediction can occur in regions where the absorption changes rapidly over short distances, such as near the rigidity cutoff latitude boundary and near the solar terminator. In this paper, the variation of absorption with solar-zenith angle,  $\chi$ , is closely examined under twilight conditions and evidence is presented of considerable variability in the rates of such twilight changes, particularly after sunrise, when daytime ionosphere conditions can be very slow to develop fully.

Variations in the daytime, night-time and twilight responses are quantified by fitting parameters to a modified empirical model which parameterizes the twilight changes separately for sunrise and sunset, and which can be used as an assimilative real-time or nowcasting model of HF radio absorption. The correlations of fitted model parameters between riometer locations and from day to day are then presented.

For the purpose of nowcasting HF radio absorption, the optimisation of parameters by regression to age-weighted riometer measurements improves accuracy compared with the use

of satellite measurements alone. This is demonstrated by an example using data from 25 riometers.

It should be noted that an additional component of CNA in the auroral zones (approximately 60-75° geomagnetic latitude) results from the precipitation of > 20 keV electrons from the magnetosphere. This auroral absorption (AA) is often localized and sporadic in nature [Foppiano and Bradley, 1983]. By analysing only the most intense solar proton events, the contribution of AA to the 5-minute median absorption measurements may be assumed negligible in comparison with the proton-produced CNA, although this assumption is less valid during weaker PCA events in the auroral zones. Verronen *et al.* [2015] demonstrated that ionization below 80 km was dominated by protons during both a large SPE (Oct-Nov 2003) and a moderate-intensity SPE (Sep. 2005). Thus the CNA originating from altitudes below 80 km should not be much affected by electrons. Riometer measurements are also subject to sporadic extraneous radio noise (e.g. man-made interference and solar radio bursts) which negatively bias the absorption measurements, and the effects of errors in quiet-day curve estimation (typically of the order of  $\pm 0.1$  dB). These errors are difficult to quantify objectively and so have been neglected in the modeling.

## 2 Theory

### 2.1 Physics-based, Full-Profile PCA Models

In full-profile PCA models, the height rate of absorption of 30-MHz radio waves,  $\partial A/\partial z$  (dB/km), is determined as a function of altitude,  $z$ , based on altitude profiles of the effective electron-neutral collision frequency,  $\nu(z)$ , and the electron density,  $N_e(z)$  [Davies, 1990, p.216]. The latter is determined by equating the rate of ionisation due to collisions and

photoionisation,  $q(z)$ , with the rate of the combined processes leading to the loss of free electrons. This is often expressed as [Hunsucker and Hargreaves, 2003, p.19-20]

$$q(z) = \alpha_{eff}(z)N_e^2(z) \quad (1)$$

where  $\alpha_{eff}$  is called the *effective* recombination coefficient, defined as

$$\alpha_{eff} \equiv (1 + \lambda)(\alpha_d + \lambda\alpha_i) \quad (2)$$

where  $\lambda$  is the ratio of negative ions to electrons,  $\alpha_i$  is the coefficient of recombination between negative and positive ions, and  $\alpha_d$  is the coefficient of recombination between electrons and positive ions. In the D-region the primary positive ions are  $NO^+$  and  $O_2^+$ . ( $N_2^+$  is also produced directly but rapidly transfers its charge to oxygen:  $N_2^+ + O_2 \rightarrow N_2 + O_2^+$ ). The principal negative ion is  $O_2^-$ .

Gledhill's [1986] review of published  $\alpha_{eff}$  measurements during SPEs and PCA events showed that their values spanned four orders of magnitude at 50-70 km altitude. Gledhill [1986] fitted exponential profiles to the measurements between 50 and 100 km, but noted that the values were "certainly not reliable to within a factor of 2 and in some cases not even to within an order of magnitude". Nonetheless,  $\alpha_{eff}$  is generally much higher at night than during the day [Hargreaves and Birch, 2005; Gledhill, 1986], such that 30 MHz CNA is approximately 5 - 7 times greater (in dB) during the day than during the night [Sellers et al., 1977].

The full-profile PCA model described in Rogers and Honary [2015] is based on [Patterson et al., 2001] but with neutral densities and temperature profiles determined from the climatological NRL-MSISE-00 model [Picone et al., 2002]. In its simplest form, fixed day- and night-time exponential profiles of  $\alpha_{eff}(z)$  are used in the D region, but the scale heights of each profile may be optimized by regression to the riometer measurements.

Predictions are also obtained from a second model, the Sodankylä Ion-neutral Chemistry (SIC) model [Verronen *et al.*, 2005]. This calculates  $q(z)$  and  $\alpha_{eff}(z)$  more precisely using density profiles of 36 positive ions, 27 negative ions and 14 neutral species (listed at <http://www.sgo.fi/SIC/>), between 50 and 150 km altitude, based on the rates of more than 400 chemical reactions. The SIC model has previously been used to model electron density profiles following PCA events with reasonable agreement with incoherent scatter radar observations [Verronen *et al.*, 2006; 2015] and observations of perturbations to the Earth-ionosphere VLF waveguide [e.g. Clilverd *et al.*, 2005].

## 2.2 Empirical PCA Models

Empirical forms of PCA model are simpler to implement in an HF nowcasting service since they omit the calculation of density, temperature and recombination rate profiles. These models instead use a statistical climatological relation between the CNA prediction,  $\hat{A}$ , and the square-root of the proton flux integrated above an energy threshold,  $J(> E_t)$ , i.e.

$$\hat{A} = m \sqrt{J(> E_t)} \quad (3)$$

The theoretical basis for this was detailed by Potemra [1972]: The proton flux-energy spectrum is approximated as a power-law,

$$J(> E) = J(> E_t) \left( \frac{E}{E_t} \right)^{-\gamma} \quad (4)$$

and  $m$  is a constant approximating a double-integral function of  $\gamma$ ,  $E_t$ ,  $\alpha_{eff}(z)$ , the electron-neutral collision frequency profile  $\nu(z)$ , and the profile of ionisation rate per unit energy,  $Q(E, z)$ , which are all assumed to be slow-varying compared with  $J(E)$ . Potemra [1972] formulated  $m$  as

$$m = \sqrt{\gamma E_t^\gamma} \int_{z=0}^{\infty} \frac{1}{\sqrt{\alpha_{eff}(z)}} \frac{1.16}{v(z)} C_{\frac{5}{2}} \left\{ \frac{\omega \pm \omega_H}{v(z)} \right\} \sqrt{\int_{E=0}^{\infty} Q(E, z) E^{-\gamma-1} dE dz} \quad (5)$$

where  $C_{5/2}\{\cdot\}$  is an integral function tabulated by *Dingle et al.* [1957],  $\omega$  is the radio frequency (radian/s) and  $\omega_H$  is the (negligible) electron gyrofrequency. Values of the threshold  $E_t$  are chosen empirically to minimize the variation of  $m$  with the spectral index,  $\gamma$ , which itself may vary over time.

A widely used model of this type is the D-Region Absorption Prediction model (DRAP), adopted by NOAA to provide global absorption maps from real-time satellite measurements [*Sauer and Wilkinson, 2008; Akmaev et al., 2010*]. DRAP chooses the values  $m$  and  $E_t$  for fully-developed day- and night-time ionospheres as:

$$m_d = 0.115 \text{ dB pfu}^{-1/2}, \quad E_{td} = 5.2 \text{ MeV}$$

$$m_n = 0.020 \text{ dB pfu}^{-1/2}, \quad E_{tn} = 2.2 \text{ MeV}$$

(applying subscripts  $d$  and  $n$  for day and night, respectively). These constants were determined empirically by *Sellers et al.* [1977] based on an analysis of four PCA events at the riometer at Qaanaaq (formerly Thule), Greenland (76.6°N, 68.7°W). The principal region of radiowave absorption in the daytime is at relatively low altitudes, reached by higher-energy protons (> 5 MeV). At night, however, the effective recombination rates at low altitudes are much higher and the principal region of absorption at night lies at higher altitudes (70-80km), ionized by 3-5 MeV protons ([*Potemra, 1972*]).

In DRAP, a further component of absorption due to solar X-ray photoionisation is added for the sunlit ionosphere using the empirical model of [*Schumer, 2009 (p.49)*].

### 2.3 The proton rigidity cutoff latitude

In all PCA models, the proton spectrum,  $J$ , must be zeroed below the rigidity cut-off energy,

$$E_c = \sqrt{E_0^2 + R_c^2} - E_0 \quad (6)$$

where  $E_0$  is the proton rest energy (938.3 MeV) and  $R_c$  is the cutoff rigidity (in MV).  $R_c$  is approximately 14.5 GV for particles arriving vertically at the geomagnetic equator and in the dipole field approximation it declines with increasing geomagnetic latitude,  $\lambda$ , as  $\cos^4(\lambda)$  [Størmer, 1955]. At high latitudes however, the field deviates from the ideal dipole form and  $R_c$  must be modeled with a dependence on geomagnetic activity and local time. In DRAP, it is determined using the *Smart et al.* [1999] model as a function of invariant latitude and the geomagnetic indices  $K_p$  and  $D_{st}$ .

#### 2.4 Modeling the twilight transition in PCA

Modeling the twilight transition in PCA nowcasts is particularly important for the high-latitude regions which spend a relatively large proportion of time in the twilight zone.

Several authors have modeled the rapid changes in ionospheric D-region chemistry that occur at twilight (see [Osepian et al., 2009] and references therein) but such information cannot be input to empirical models such as DRAP, which are intended for real-time application.

DRAP takes a heuristic approach to determining absorption in the twilight region. The absorption estimate is a linear interpolation between  $A_d$  and  $A_n$  based on the solar zenith angle,  $\chi$ , which may be expressed as

$$\hat{A} = A_n(1 - Z_d) + A_d Z_d \quad (\text{dB}) \quad (7)$$

where  $Z_d$  is a ‘daytime weighting’ factor given by

$$Z_d(\chi) = \begin{cases} 1, & \chi \leq \chi_l \quad (\text{day}) \\ \frac{(\chi_u - \chi)}{(\chi_u - \chi_l)}, & \chi_l < \chi < \chi_u \quad (\text{twilight}) \\ 0, & \chi \geq \chi_u \quad (\text{night}) \end{cases} \quad (8)$$

In DRAP, the transition region is bounded by  $\chi_l = 80^\circ$  and  $\chi_u = 100^\circ$  and these bounds are the same for both sunrise and sunset. However, for a given proton flux, the ionospheric absorption response,  $A(\chi)$ , is known to differ between sunrise and sunset – a phenomenon known as the “Twilight anomaly” [Reagan and Watt, 1976; Ranta et al., 1995; Hargreaves et al., 1993; Sauer, 1968; Stauning, 1996; Chivers and Hargreaves, 1965]. The physical causes, discussed in Section 4, relate to complex changes in the altitude profile of plasma composition and ion-exchange reaction rates at twilight. Past researchers have particularly focused on the rapid transitions near the Earth shadow line (or solar terminator) as it passes through the D-region ionosphere at  $\chi \approx 98^\circ$  [Osepian et al., 2008, 2009; Collis and Rietveld, 1990; Reagan and Watt, 1976]. However, there have been very few studies of the more gradual ionospheric changes pre-sunset or post sunrise ( $\chi < 90^\circ$ ).

Full-profile PCA models may model the twilight transition using the ‘Earth shadow’ method to select day or night-time of the effective recombination coefficient profile,  $\alpha_{\text{eff}}(z)$  based on whether or not it is solar-illuminated. However, this method does not reproduce the slow ionospheric response (particularly for  $\chi < 90^\circ$ ) and produces large errors in absorption predictions at twilight.

## 3 Results

### 3.1 Optimal PCA Model Parameters for Day and Night Conditions

The [Sellers *et al.*, 1977] parameters  $m_d$ ,  $m_n$ ,  $E_{td}$ , and  $E_{tn}$  used in DRAP may be assessed by comparison with measurements from other polar-cap riometers and a large selection of SPEs. Measurements from the four highest latitude riometers in the Canadian NORSTAR riometer array are examined for 13 intense multi-day SPEs in 1998-2005 (see Table 2). (This selection matches those of Rogers and Honary [2015] and Akmaev *et al.* [2010]). The locations of the four riometers – Taloyoak, Contwoyto Lake, Rankin Inlet, and Eskimo Point – are given in Figure 1 and Table 1.

CNA measurements (5-minute medians) were filtered to remove (i) calibration signals, (ii) periods within 3-hours of the start of the SPE (when the solar proton pitch angle distribution may be anisotropic [Koutsnetsov *et al.*, 2014]), (iii) times up to 15 minutes before and six hours after geomagnetic storm sudden commencements or sudden impulses, and (iv) short periods affected by obvious artefacts. Integral solar proton fluxes were determined from the energetic particle sensors on the GOES-8 satellite (up to 17 June 2003) or GOES-11 (from 19 June 2003), integrated above energy thresholds of 1, 5, 10, 30, 50, 60 and 100 MeV and interpolated for intermediate threshold energies,  $E_t$ , assuming the power law of Equation (4).

Values of  $m_d$  and  $m_n$  minimising the root-mean-squared error (RMSE) in CNA are presented in Figure 2a and b respectively for a range of energy thresholds,  $E_t$ . Solid lines represent optimisations for individual riometers, whilst the dashed line represents an optimisation of the combined 4-riometer data set. Data for twilight conditions are excluded over a wide margin by defining daytime conditions as  $\chi < 60^\circ$  and night as  $\chi > 120^\circ$ . The corresponding RMSEs of the model (Equation (3)) presented in Figure 2c and d show that the

optimal threshold energy,  $E_t$ , differs between riometers, varying from 2.7 to 8.7 MeV (day) or 1.2 to 2.2 MeV (night). Figure 2 shows a large variation in the optimum  $m_d$  and  $m_n$  parameters, differing by approximately  $\pm 30\%$  between riometer locations. For comparison, the fixed parameters of the DRAP model [Sellers *et al.*, 1977] – shown as asterisks in Figure 2 – are generally higher than optimal, and so tend to overestimate CNA at these locations.

The optimum parameters (calculated for individual riometers and for the combined 4-riometer data set) are listed in Table 3 (columns 2-3) together with the associated minimum RMSE (column 4). The associated RMSEs of the DRAP model are shown in column 5 of Table 3 and can be considerably higher than for the optimized model—between 6% and 143% higher.

The threshold model (Model A) makes use of integral proton flux measurements from only two of the seven energy thresholds provided in the GOES SEM data set. (For example,  $J(>5.2 \text{ MeV})$  is determined from  $J(>5 \text{ MeV})$  and  $J(>10 \text{ MeV})$  only.) To utilize more of the available information from GOES, an alternative PCA model (Model B) was trialled in which the CNA prediction,  $\hat{A}$ , is formed as a linear weighted sum

$$\hat{A} = \sum_{i=1}^7 m_i \sqrt{J(> E_i)} \quad (\text{dB}) \quad (9)$$

where  $m_i \geq 0$  are optimized coefficients and  $E_i$  are the corresponding energy thresholds (1, 5, 10, 30, 50, 60 and 100 MeV). In most cases this model produced only marginal improvement in RMSE, with minimum RMSE values (shown in column 6 of Table 3) lying within 4% of the Model A values in all but one case (the Contwoyto Lake, daytime dataset, which gave a 15% improvement for Model B). Parameter optimisations were required for

only two or three channels to achieve convergence. In the case for which data is assimilated from all four riometers, for daytime ( $\chi < 60^\circ$ ) Model B (Equation (9)) was optimized as

$$\begin{aligned}\hat{A}_d &= 8.28 \times 10^{-2} \sqrt{J(> 5MeV)} \\ &+ 6.63 \times 10^{-2} \sqrt{J(> 100MeV)}\end{aligned}\tag{dB} \quad (10)$$

whilst for night ( $\chi > 120^\circ$ ) the best-fit parameterisation was

$$\begin{aligned}\hat{A}_n &= 8.19 \times 10^{-3} \sqrt{J(> 1MeV)} \\ &+ 4.78 \times 10^{-3} \sqrt{J(> 10MeV)} \\ &+ 9.79 \times 10^{-4} \sqrt{J(> 30MeV)}\end{aligned}\tag{dB} \quad (11)$$

with  $J$  in units of pfu.

These results indicate that inclusion of flux measurements for all energy channels (Model B) produces only a very marginal improvement in the optimisations for day or night conditions achieved by the simpler threshold model (Model A).

### 3.2 Optimizing the twilight transition model

In this section an empirical PCA model is developed with variable day, night and twilight parameters to examine how the best-fit parameters at each location vary over the course of SPEs and between SPEs, and how these variables correlate between riometer locations in the Canadian region.

The simple three-line twilight transition (Equation (8)) used in the DRAP model is shown as the solid blue line in Figure 3.

The dashed curve in Figure 3 represents an alternative, smooth form of the daytime weighting function ( $Z_d(\chi)$ ) given by

$$Z_{ds}(\chi) = \frac{1}{2} \left( 1 - \operatorname{erf} \left( \frac{\chi - \frac{1}{2}(\chi_u + \chi_l)}{\frac{1}{2}(\chi_u - \chi_l)} \right) \right) \quad (12)$$

where  $\operatorname{erf}()$  denotes the Gauss error function. This avoids the discontinuities at  $\chi_u$  and  $\chi_l$  and provides a closer fit to the measurements.

In Figure 4, the marker points indicate the quantity

$$m_5 = A/\sqrt{J(> 5 \text{ MeV})} \quad (13)$$

measured at the riometer at Fort Churchill, Canada (58.8°N, 265.9°E) separately for a) pre-noon and b) post-noon local time (LT) periods for the multi-day SPE of April 2002.

The distributions of  $m_5$  indicate that the weighting function  $Z_{ds}(\chi)$  provides an appropriate form for the twilight transition but during this event the chosen limiting values of  $\chi_l = 80^\circ$  and  $\chi_u = 100^\circ$  assumed in the DRAP model would be better modified to approximately  $70^\circ$  and  $98^\circ$  respectively for sunrise, and  $88^\circ$  and  $100^\circ$  respectively at sunset. The points in Figure 4 are colored separately for each day of the SPE and demonstrate a large day-to-day variation in the values of the night and day values of  $m_5$  (These shall again be denoted  $m_n$  and  $m_d$ , respectively, but note that both now relate to a 5 MeV threshold).

The solid lines superposed in Figure 4 represent the optimally parameterized fit of the function

$$\hat{m}(\chi) = m_n(1 - Z_{ds}(\chi)) + m_d Z_{ds}(\chi) \quad (14)$$

This function is fitted using a trust-region-reflective algorithm [Coleman and Li, 1996] with initial and limiting parameter values as given in columns 1-4 of Table 4. This algorithm is

effective in performing sum-squared-error minimization on a smooth nonlinear function of many variable parameters, subject to upper and lower bounds on the variables. It is a modification of the familiar Newton method in which parameters are optimized iteratively (within certain constraints) until either the sum of residuals is less than a tolerance threshold of  $10^{-6}$  dB<sup>2</sup> or the maximum change in each variable value is less than a threshold of  $10^{-6}$ .

The function fit was rejected (and not shown in Figure 4) except in the following circumstances:

- There was a wide range of solar-zenith angles, with  $\min(\chi) < 80^\circ$  and  $\max(\chi) > 100^\circ$  ;
- The number of measurement points was greater than ten;
- The Pearson correlation coefficient,  $r$ , of the fit exceeded 0.9;
- The p-value [Fisher, 1970] was less than 0.05 (at the 5% significance level), indicating a low probability that  $r$  was obtained by random chance;
- Fitted parameters  $\chi_l$  and  $\chi_u$  were not near the extreme values of the data set (specifically,  $\chi_l > \min(\chi) + 2^\circ$  and  $\chi_u < \max(\chi) - 2^\circ$  ); and
- Fitted parameters were not at the limits of their range (columns 3 and 4 of Table 4).

Fitting of the model function (Equation (14)) was repeated for the four riometers (talo, cont, rank, and eski – which are located well inside the polar cap ( $L > 10$ ) – and for the 13 selected SPEs. (However, model fitting for 4 SPEs near the solstices was not possible using the rule-base above due to the limited zenith angle range.) The selection of polar cap riometers minimizes the effects of both the proton rigidity cutoff (which varies with magnetic local time) and any contributions to absorption from electrons precipitated from the outer Van Allen belt ( $L=4-6$ ). The resulting best-fit parameters are shown in Figure 5a for sunrise and

Figure 5b for sunset, where the red '+'s indicate the parameters  $(\chi_l, m_d)$  and blue '×'s the parameters  $(\chi_u, m_n)$ .

The means and standard deviations (SD) of the four fitted parameters are presented in the last two columns of Table 4. Fitted values for  $\chi_l$  have a smaller mean and greater standard deviation post-sunrise compared with pre-sunset. Fitted values for  $\chi_u$  also exhibit a slightly smaller mean pre-sunrise compared with those post-sunset.

### 3.3 Comparison with the 'Earth Shadow' method (full-profile PCA models)

For full-profile PCA models, an 'Earth shadow' method is often used to model the twilight transition. To illustrate this technique, Figure 6 presents an example of the time-varying profiles of a) electron density,  $N_e(t, z)$ , and b) the height rate of absorption,  $\partial A/\partial z$  (dB/km), at the Taloyoak riometer for the SPE of 20-24 April 1998, calculated from the *Rogers and Honary* [2015] full-profile model. The right vertical axes in Figure 6 indicate the solar-zenith angle associated with the Earth's shadow at each altitude, given approximately by

$$\chi = \sin^{-1} \left( \frac{R_E}{(R_E + z)} \right) \quad (15)$$

(neglecting refraction), where  $R_E$  is the Earth radius. The hyperbolic discontinuities (or 'cut-outs') in the low-altitude profiles at night result from the use of the night-time  $\alpha_{eff}(z)$  profile at altitudes for which the ionosphere is in the Earth's shadow and daytime  $\alpha_{eff}(z)$  profiles elsewhere. The scale height of the E region ( $> 85$  km) is a constant 51 km [Vickrey *et al.*, 1982], whilst that in the D-region  $\alpha_{eff}(z \leq 85$  km) is determined by regression to the complete set of riometer measurements for this SPE, giving best-fit values of  $h_{Dn} = 2.11$  km (night) and  $h_{Dd} = 5.77$  km (day).

Integrating the absorption rate profile of Figure 6b in altitude results in the CNA prediction of Figure 7a (green line). This is plotted alongside the riometer measurements (black line), and predictions of the DRAP empirical model (blue dashed line). The Earth-shadow method substantially overestimates the absorption level in the twilight regions, with the predicted sunrise transitions commencing approximately 3.6 h too early (at  $\chi \sim 96^\circ$  rather than  $\sim 82^\circ$ ) and sunset transitions commencing 2.0-2.7 h too late (at  $\chi \sim 96^\circ$  instead of  $86-90^\circ$ ). The magnitude of the discrepancy is made clear in Figure 7b in which the model predictions are plotted directly against the riometer measurements.

A more gradual twilight transition could be modeled by replacing the Earth shadow method with the  $\alpha_{eff}(z, \chi)$  profiles of *Reagan and Watt* [1976] or *Osepian et al.* [2009]. However, these are defined only in the interval  $\chi = 90-98^\circ$  and their form would need to be parameterized to allow them to be optimized for each event in real-time. An approximation to this technique was tested by replacing the Earth-shadow technique with a method in which the predictions for day and night profiles  $\alpha_{eff}(z)$  are combined using the linear weighting factor  $Z_d(\chi)$  of Equation (8) (with  $\chi_l = 80^\circ$  and  $\chi_u = 100^\circ$  as in DRAP). The resulting predictions (the red line in Figure 7) are a much closer fit to the measurements although it is clear that the DRAP parameters still require optimization. (For example, the modeled sunset transition still begins 1-2 h earlier than the measurements indicate, suggesting that  $\chi_l = 80^\circ$  is  $5-10^\circ$  too low for the sunset transition).

Any full-profile model using either the Earth shadow technique or  $\alpha_{eff}(z, \chi)$  profiles defined only above  $\chi \geq 90^\circ$  will fail to represent slowly-varying ionospheric compositional or temperature changes which affect the absorption response pre-sunset and particularly post-sunrise for  $\chi < 90^\circ$ .

As a comparison, the SIC model was used to model profiles of the specific absorption,  $\partial A/\partial z$ , at Fort Churchill for this SPE and vertical integration of such profiles provides a reconstruction of the expected CNA (see Figure 8). The SIC model simulates the diurnal and SPE-driven changes in oxygen species ( $O$ ,  $O_2(^1\Delta_g)$ , and  $O_3$ ), which are important for the modeling of sunset effects as discussed in [Verronen *et al.* 2006]. It also models enhancements of  $NO$  as the SPE develops, the amount of which is important for the smoothness of the twilight transition (as shown for  $\chi > 80^\circ$  in [Verronen *et al.* 2006]) because greater  $NO$  concentrations produce stronger dependence to reactions driven by UV radiation. A constant proton flux was used in the SIC calculations to facilitate a direct comparison with the normalized measurements shown in Figure 4. Pre-noon periods are colored green and post-noon blue and the predictions are plotted against (a) date, (b) Universal Time (all days superposed) and (c) solar-zenith angle ( $\chi$ ). The SIC model predicts a rapid rise in the absorption at  $\chi \sim 98^\circ$  (corresponding to Earth's shadow passing through the D-region ionosphere at 55 - 71 km altitude—near the height of maximum  $\partial A/\partial z$  in the daytime ionosphere) with a more gradual change between  $\chi = 85^\circ - 97^\circ$ . The post-sunrise predictions (the green points in Figure 8c) are slightly lower than those pre-sunrise (blue) for the same values of  $\chi$  but this is a less marked difference than that observed in the measurements and the difference is negligible below around  $\chi = 83^\circ$ . The SIC model predictions of CNA for constant proton flux spectrum,  $J(E)$ , should be proportional to the value  $m$  observed in the riometer measurements. However, the day-to-day variability in  $m$  of approximately  $\pm 30\%$  evident in Figure 4 is not reproduced in the SIC model predictions.

Two more sensitivity studies were conducted with the SIC model in an attempt to replicate the anomaly between sunrise and sunset ionospheric absorption responses: Changing the attachment rate (which is equivalent to changing the temperature) by 20% had negligible effect. However, changing all rates of electron detachment reactions in the model—which depend on both ultraviolet (UV) and/or visible solar radiation (see [Verronen *et al.*, 2006])—to scale with UV flux only (wavelength < 318 nm) produced a smoother  $A(\chi)$  transition over  $\chi = 80^\circ - 100^\circ$  similar to that seen in the sunset observations (Figure 4b). Nevertheless, the modeled sunrise transition did not extend to  $\chi < 80^\circ$ , as seen in the observations (Figure 4a), which seems to indicate that the sunrise time scales and the sunrise/sunset asymmetry in riometer absorption cannot be explained by the modeled ion chemistry.

### 3.3.1 Antenna aperture averaging

PCA models provide predictions of CNA for a narrow zenithal beam, whereas the Canadian riometer measurements employed four-element wide-beam antennas which illuminated a region of ionosphere approximately 100 km in radius, centred on the zenith [Rostoker *et al.*, 1995, p.751]. This corresponds to a range of zenith angles up to  $\pm 0.9^\circ$ . There is therefore some aperture averaging inherent in the measured  $m_5(\chi)$  profiles of Figure 4 but this is not sufficient to explain the large discrepancy between measurements and the SIC model predictions. An indication of the scale of this difference may be observed by comparing CNA measurements from coaxial vertical beams of different beamwidths. In Figure 9, the blue lines present data for the narrow central beam of the IRIS imaging riometer at Kilpisjärvi, Finland, (3-dB beamwidth =  $12.8^\circ$  [Honary *et al.*, 2011]) whilst the red points present the absorption from the wide beam ( $60^\circ$  width) formed from a single crossed-dipole

antenna at the same location. This widebeam antenna— supplied by La Jolla Sciences of Solana Beach, California—is also used by riometers of the NORSTAR array.

CNA measurements for both beams were calibrated using tables of effective obliquity factors [Hargreaves and Detrick, 2002] for each beam, to give an estimate of absorption expected on the zenithal line. With this calibration, the measurements agree to within approximately 0.1 dB. A 24-h sample of CNA measurements (from local noon 21 April 1998) plotted against zenith angle in Figure 9b indicates comparative aperture averaging no greater than approximately  $\pm 1^\circ$  of zenith angle.

#### 3.4 The covariance of optimal PCA model parameters

In developing a nowcast empirical PCA model it is instructive to analyse the covariance of the parameters both spatially (between riometer locations) and temporally (during a SPE and between events). The fitted values  $\chi_l$ ,  $m_d$ ,  $\chi_u$  and  $m_n$  presented in Figure 5 have been replotted as time series in Figure 10, with sunrise values on the left and sunset values on the right. (Note that, unlike Figure 5, Figure 10 also includes a small number of points for which parameters were found to be optimum at the upper and lower limits of the allowed range.) For clarity, only the first 5 days of each SPE are presented (omitting only 9 of 166 fits from days 6 or 7 of an event). The commencement date for each SPE is noted at the top of each figure and each colored line represents a different riometer in the polar cap region.

This representation shows that model parameters fitted for different riometers often follow a similar pattern of variation during each SPE. The correlations are weak in general, but the sign of day-to-day changes in parameter values are often the same for multiple riometers.

This is in part due to the expected uniformity of the energy spectrum of precipitating solar

protons across the region (at least for the dayside polar cap after the first few hours of the SPE [Kouznetsov *et al.*, 2014]). A change in the proton flux spectral index,  $\gamma$ , will lead to changes in the  $m$  parameter for example, although this variance should be minimal when  $E_t$  is correctly optimized. If the energy threshold estimate  $\hat{E}_t$  ( $=5$  MeV in the present model) is too high at a particular riometer location, the measured  $m$  will increase with increasing  $\gamma$ , but if  $\hat{E}_t$  is too low, the measured  $m$  will decrease with increasing  $\gamma$ . This effect was modeled and presented in Figures 2 and 3 of Sellers *et al.* [1977] or Figure 1 of Potemra [1972]. The covariance of optimal parameters may also be partly due to similarities in the profiles of mesospheric chemical composition and temperature at each location, since these determine the twilight response function.

Assumptions of uniformity could form the basis for extending real-time PCA models for the whole polar-cap region, based on assimilation of measurements from a small number of riometers. However, it is clear that assimilation of data from only a single riometer would yield unsatisfactory results due to (i) the variation between optimal  $E_t$  and  $m$  values for the riometer (discussed in Section 3.1), (ii) inaccuracy in the riometer's calibration (e.g. in the quiet-day curve estimate) and (iii) the presence of extraneous noise or local radio interference at that riometer site. A real-time absorption model should therefore assimilate data from multiple widely distributed riometers to reduce the effect of these local error sources.

The median proton fluxes  $J(> 10 \text{ MeV})$  associated with each data point in Figure 10 are presented in Figure 11 a) for sunrise and c) sunset. Assuming a power-law proton flux spectrum of the form in Equation (4), Figure 11b) and d) represent median values of the spectral index,  $\gamma$ , (for sunrise and sunset respectively), measured from two integral proton flux measurements,  $J(> 10 \text{ MeV})$  and  $J(> 30 \text{ MHz})$ :

$$\gamma_{(10,30MeV)} = \frac{\log(J(> 10 MeV)) - \log(J(> 30 MeV))}{\log(10) - \log(30)} \quad (16)$$

Most SPEs are characterized by both a declining proton flux (after peaking on Day 1 or 2) and an increasing spectral index, indicating a more rapid decline in the more energetic protons. However, further analysis (not presented) revealed no strong correlation of the variables  $m_n$ ,  $m_d$ ,  $\chi_u$ , or  $\chi_l$  with  $\gamma_{(10,30MeV)}$ ,  $\gamma_{(5,10MeV)}$  or  $J(> 10 MeV)$ , based on their median values in the 12-hour periods studied. Similarly, neither the month of occurrence nor the peak flux  $J(> 10 MeV)$  of each entire SPE were strong indicators of the four twilight model parameters.

Correlation coefficients of  $m_n$ ,  $m_d$ ,  $\chi_u$ , or  $\chi_l$  are presented in Figure 12 based on pairs of riometers in the “Churchill line” – a line of seven riometers (talo, rank, eski, fchu, gill, isll and pina) close to the 94°W meridian (see Figure 1). Red shading indicates positive correlation, blue indicates negative correlations, and since the riometers are ordered by latitude, coefficients for the more closely spaced riometers are shown nearer to the leading diagonal. These figures indicate that the correlation of  $m_d$  and  $m_n$  between neighboring riometers is higher than for more distant riometers. This is in part due to the higher proton rigidity cutoff at lower latitudes and the contribution of auroral absorption from energetic electrons. Even so, the sunrise values  $\chi_l$  (left panel of Figure 12c) are all positively correlated, though sometimes only weakly.

### 3.5 Example of real-time PCA model optimization

This section presents an example in which the parameters of a PCA model (PCAM) are optimized in real time by assimilating measurements from 25 of the riometers in the NORSTAR, NRCan and SGO arrays which were operational in March 2012. The model—an

extension of the ‘Type 1’ model detailed in *Rogers and Honary* [2015]—estimates CNA at 30 MHz using Equation (7), optimising parameters  $m_n$ ,  $m_d$ ,  $\chi_u$  (sunrise and sunset),  $\chi_l$  (sunrise and sunset) and a variable correction,  $\Delta\lambda$  to the rigidity cutoff geomagnetic latitude determined from the [*Smart et al.*, 1999] model (as used in DRAP) based on geomagnetic indices  $D_{st}$  and  $K_p$ . Threshold energies  $E_{tn}$  and  $E_{td}$  retain their constant DRAP values of 2.2 and 5.2 MeV respectively. The optimization is performed by regression to the riometer measurements of CNA, with each measurement exponentially age-weighted with a characteristic decay time of 24 hours. For the few riometers not operating at 30 MHz, the absorption measurements are adjusted assuming an  $f^{-1.5}$  frequency dependence. The exponent of 1.5—which was also used in the DRAP model—is in agreement with exponents from 1.4 to 1.6 presented in Figure 10 of *Patterson et al.* [2001] derived from three SPEs in 1989-1990. The value differs from the exponent of 2 familiar from generalized magnetoionic theory because the electron-neutral collision frequency is non-negligible (relative to the radio wave frequency) below 70 km during PCA events (see e.g. [*Rosenberg et al.*, 1991]).

The values of the optimized parameters during the course of an SPE in March 2012 are presented in Figure 13. There is a high variance during the first several hours of the event since the number of data points in the assimilation is initially small. Thereafter it is interesting to note the value of the optimal equatorward shift  $\Delta\lambda$ , in the rigidity cutoff, which increases to several degrees during the course of the event (see panel c). The value of  $\chi_l$  (sunrise) (see panel b) is much more variable and generally lower than its sunset value for most of the event.

The RMS and mean error (bias) of the optimized model are presented for each riometer location in Figure 14a (dash lined) alongside the predictions of the unoptimized DRAP model (solid lines). The riometers are ordered by geomagnetic latitude as shown in Figure 14b. The optimisation reduces RMSE and bias at nearly every location, with the greatest improvements

observed in the central latitude zone (64-72° geomagnetic) where reductions in RMSE of more than 30% are observed. The particular improvement in this latitude zone may be largely due to the improved location of the rigidity cutoff boundary, optimisation of which has less effect at higher or lower latitudes. Optimisations not including the variable rigidity cutoff latitude parameter  $\Delta\lambda$  (not shown) improved the model bias and RMSE to a lesser amount in this latitude zone.

#### 4 Discussion

Modeling the changes in ionospheric CNA at twilight is a particular challenge since effective recombination coefficients,  $\alpha_{eff}$ , can vary by an order-of-magnitude in the lower D-region [e.g. *Gledhill*, 1986] due to changes in ionospheric constituent concentrations, temperatures and transport rates. After sunrise, the principal negative ion  $O_2^-$  in the night-time D-region undergoes photodetachment by visible light [*Hunsucker and Hargreaves*, 2003, p.402], and below 70 km altitude, further dissociation of  $NO_3^-$  is an important source of free electrons. This ion ( $NO_3^-$ ) has a high affinity for electrons and requires UV light to photodissociate, although this process can be delayed at sunrise due to the screening of UV solar radiation by an underlying stratospheric ozone layer. Atomic oxygen plays an important role in the formation of  $NO_3^-$  [*Osepian et al.*, 2008] and there may be slow build-up of  $O$  after sunrise which may potentially delay the rise in CNA [e.g. *Collis and Rietveld*, 1990]. However, the concentration of  $O$  is rapidly diminished through reactions with odd Hydrogen constituents  $OH$  and  $HO_2$ , whose concentrations increase during an SPE [*Osepian et al.*, 2008]. Several researchers have modeled the sunrise and sunset changes in the  $\alpha_{eff}(z)$  profile for  $\chi$  between 90° and 98° and described the evolution of these profiles during selected SPEs (e.g. *Osepian et al.* [2009] and *Reagan and Watt* [1976]). The asymmetry between patterns of  $\alpha_{eff}(\chi)$  between sunrise and sunset for  $\chi > 90^\circ$  has been well reported as a “Twilight

Anomaly". This was reviewed by *Reagan and Watt* [1976], who found that the value of  $\alpha_{eff}$  below 80 km altitude at sunset only began to reduce when  $\chi$  exceeded  $94^\circ$ , and that this was consistent with the persistence of atomic oxygen (which has a lifetime of approximately 45 minutes at 70 km altitude). At sunrise, however, the production of  $O$  and  $O_2(^1\Delta_g)$  from UV photodissociation of  $O_3$  is more rapid (a lead time of approximately 10 minutes). *Stauning* [1996] postulated that a  $1^\circ$  difference in  $\chi$  observed at the transition to steady night-time absorption of the change at sunrise and sunset ( $97.5^\circ$  and  $98.5^\circ$  respectively) for the 31 Oct. 1992 PCA event may be explained by a rise in the effective absorption heights of a few km (potentially due to heating of the atmosphere during the day). The changing distribution of  $\chi_u$  values presented in Figure 5 (increasing from a mean solar-zenith angle of  $97.9^\circ$  at sunrise to  $100.6^\circ$  at sunset) are, therefore, consistent with these earlier descriptions of the Twilight Anomaly.

However, the profile of CNA at  $\chi < 90^\circ$  has been much less frequently discussed in the literature. A delayed post-sunrise response was observed from riometer records at Thule, Greenland and Great Whale River, Canada ( $55.3^\circ\text{N}$ ,  $77.8^\circ\text{W}$  geodetic) [*Sauer*, 1968] in which the absorption was not fully developed after sunrise (relative to a sunlit South Pole station observation) even at  $\chi=70^\circ$ , and the sunrise increase was much slower than the sunset decrease. The delay in the post-sunrise increase in absorption would result from a progressive decrease in the  $\alpha_{eff}$  profile throughout the day as observed by *Hargreaves et al.* [1987] for the 16 February 1984 PCA (single-day) event using riometers and measurements from the EISCAT incoherent scatter (IS) radar. It was determined that values of  $\alpha_{eff}$  at heights between 70 km and 85 km decreased over 3 hours as  $\chi$  reduced throughout the morning. Similarly, *Reagan and Watt* [1976] studied the August 1972 PCA using the Chatanika, Alaska IS radar ( $65.1^\circ\text{N}$ ,  $147.5^\circ\text{W}$ ) and observed a slight decrease in  $\alpha_{eff}$  progressively throughout the day at several altitudes. These changes could arise from various

factors, such as changes in local oxygen and ozone concentrations, which can develop for hours after sunrise (see Figures 32 and 33 of [Swider, 1977]), and due to local transport processes.

For locations near the edge of the polar cap, the ‘midday recovery’ phenomenon (a reduction in CNA in the few hours around local noon [Ranta *et al.*, 1995; Hargreaves *et al.*, 1993; Zmuda and Potemra, 1973] may also contribute to absorption decreases towards midday (and recovery afterwards). This has been attributed to an increase in the latitude of the rigidity cutoff boundary on the dayside resulting in proton flux that may be lower than observed on the equatorial GOES satellite (see e.g. Figure 5 of Dmitriev *et al.* [2010]).

Finally, it should be noted that absorption during PCA events may be complemented by energetic solar electrons [Potemra and Zmuda, 1972; Potemra, 1972] whose flux may vary relative to that of protons, and which are subject to different rigidity cut-offs [Dmitriev *et al.*, 2010]. The contribution to absorption from precipitating alpha particles is small compared to that of protons [Potemra and Zmuda, 1972; Baker *et al.*, 1974].

## 5 Conclusions

Empirical PCA models relate 30 MHz cosmic noise absorption ( $A$ ) to energetic solar proton fluxes during solar proton events (SPE) based on the relation  $A = m\sqrt{J(> E_t)}$ , where  $m$  and threshold energy  $E_t$  are selected for fully-developed day or night ionospheres so as to minimize the error variance with temporal changes in the hardness of the flux-energy spectrum  $J(E)$ . This paper presented an assessment of riometer measurements at four polar-cap locations during 13 large multi-day SPEs in the period 1998-2005:

- Optimal values of  $E_t$  were found to vary between riometers, from 2.74 to 8.65 MeV under daytime conditions, or from 1.19 to 2.22 MeV at night. These values are broadly consistent with those proposed by *Sellers et al.* [1977] (5.2 MeV and 2.2 MeV for day and night respectively) which form the basis of the widely used DRAP model [*Akmaev et al.*, 2010].
- The associated optimal values of  $m$  varied substantially between riometers under daytime conditions (from 0.063 to 0.122 dB pfu<sup>-1/2</sup>) with less variation at night (0.011 to 0.015 dB pfu<sup>-1/2</sup>). In all but one case these  $m$  values were lower than those in DRAP (0.115 and 0.020 dB pfu<sup>-1/2</sup> for day and night respectively).
- An optimization of parameters based on data from all four riometer locations reduced RMSE by up to 48% (daytime) or up to 59% (night) compared to predictions using the DRAP parameters.
- A further model incorporating GOES integral proton flux measurements from all 7 energy channels yielded only marginal further improvements in RMSE (typically less than 4% further improvement).
- The rapid change in  $m$  at twilight is well modeled using a simple linear day/night weighting (or a similar Gauss error-function weighting function,  $Z_{ds}(\chi)$ ) based on the zenith angles between limiting values  $\chi_l$  and  $\chi_u$ . The  $Z_{ds}$  model was fit to riometer data in 12 hour local time periods pre- or post-noon with a fixed  $E_t$  of 5 MeV. This gave optimal  $\chi_u$  at 97.9° (mean value) at sunrise compared with 100.6° at sunset. The more delayed response at sunset is consistent with previously reported observations of a Twilight Anomaly.
- The fitted values of  $\chi_l$  were highly variable and much lower at sunrise ( $73.8^\circ \pm 7.21^\circ$ ) compared with sunset ( $82.6 \pm 4.57^\circ$ ).

Examination of the correlation of the  $Z_{ds}$  twilight model parameters was examined for a chain of seven riometers along the  $94\pm 2^\circ\text{W}$  meridian. This showed that the day and night values of  $m$  were more highly correlated for closely spaced riometers. The  $\chi_l$  parameter was positively correlated for all pairs of riometers in the chain.

The twilight transition was also modeled using two full-profile physics-based models of the ionosphere. These models adopt separate  $\alpha_{eff}(z)$  profiles for day and night, depending on the Earth shadow height. An example from the SPE of April 1998 at Taloyoak, Canada showed that use of the Earth shadow method overestimated CNA during twilight, predicting a rapid rise in absorption at sunrise commencing 3.6 h too early (at  $\chi = 96^\circ$  rather than  $82^\circ$  in the measurements) and sunset transitions were predicted to commence 2 - 2.7 h too late (at  $96^\circ$  rather than  $86\text{-}90^\circ$  observed). Replacing the technique with a linear day-night weighting (as used in the empirical model) improves the fit to the measurements although the parameters of the weighting function need to be optimized in real-time. The SIC model was used to simulate changes in the ionospheric chemistry and electron attachment and detachment rates during an SPE, but these modifications were not sufficient to replicate the slow ionospheric response at sunrise ( $\chi < 80^\circ$ ) and the large sunrise/sunset asymmetry observed in riometer measurements.

In the past decade the number of riometers deployed in the high latitude regions has greatly increased (particularly in Canada), with many providing real-time measurements suitable for nowcast CNA modeling. An example was presented in which data from 25 riometers was assimilated using suitable age-weighting and variable corrections for the rigidity cutoff latitude and the twilight model parameters (optimized independently for sunrise and sunset). This demonstrated reductions of up to around 30% in RMSE compared with predictions from DRAP.

## Acknowledgments

This work was funded by UK Engineering and Physical Sciences Research Council grants EP/K007971/1 and EP/K008781/1. A. Kero was supported by the European Regional Development Fund (Regional Council of Lapland, decision number A70179). The work of P.T. Verronen was funded by the Academy of Finland project 276926 (SECTIC: Sun-Earth Connection Through Ion Chemistry).

The authors wish to thank Prof. Esa Turunen (SGO) for helpful discussions and assistance.

Operational support for the CANOPUS / NORSTAR instrument array was provided by the Canadian Space Agency. We acknowledge the efforts of Don Wallis who was principally responsible for the scientific operation of the CANOPUS riometer array and the NORSTAR team for providing the riometer data used in this study, which are available from

<ftp://aurora.phys.ucalgary.ca/data/riometer/>. SGO riometer measurements are available from <http://www.sgo.fi/Data/Riometer/rioData.php> and IRIS (Kilpisjärvi) riometer data are available from and <http://spears.lancs.ac.uk/data/request.html>. NRCan riometer data is provided as a dataset in Supporting Information and is also available on request from [Donald.Danskin@Canada.ca](mailto:Donald.Danskin@Canada.ca). We also acknowledge the US National Geophysical Data Centre for providing GOES satellite data, available from <http://satdat.ngdc.noaa.gov/sem/>, and  $K_p$  geomagnetic and solar activity indices, available from <ftp://ftp.ngdc.noaa.gov>.  $D_{st}$  geomagnetic indices were provided by the World Data Centre for Geomagnetism, Kyoto (<http://wdc.kugi.kyoto-u.ac.jp/dst/dir/>).

## References

- Akmaev, R. A., A. Newman, M. Codrescu, C. Schulz, and E. Nerney (2010), DRAP Model Validation: I. Scientific Report. Available online: [www.ngdc.noaa.gov/stp/drap/DRAP-V-Report1.pdf](http://www.ngdc.noaa.gov/stp/drap/DRAP-V-Report1.pdf).
- Bailey, D. K. (1964), Polar Cap Absorption, *Planet. Space Sci.* 12, 495-541. doi: 10.1016/0032-0633(64)90040-6.
- Baker, M. B., A. J. Masley, and P. R. Satterblom (1974), Simultaneous satellite and riometer studies. [for solar cosmic ray events], In: *International Cosmic Ray Conference, 13th, Denver, Colo., August 17-30, 1973, Proceedings. Vol. 2. (A74-30143 13-29) Denver, University of Denver, 1974, p. 1440-1445.*
- Browne, S., J. K. Hargreaves and B. Honary (1995), An imaging riometer for ionospheric studies, *Electronics & Communication Engineering Journal* 7(5), 209-217, doi: 10.1049/ecej:19950505.
- CANOPUS, (2005), CANOPUS Quiet Day Curve Generation. Available online: [aurora.phys.ucalgary.ca/norstar/rio/doc/CANOPUS\\_Riometer\\_Baselining.pdf](http://aurora.phys.ucalgary.ca/norstar/rio/doc/CANOPUS_Riometer_Baselining.pdf), University of Calgary, Canada.
- Chivers H. J. A., and J. K. Hargreaves (1965), Conjugate Observations of Solar Proton Events: Delayed Ionospheric Changes During Twilight, *Planet. Space Sci.* 1965, Vol. 13, pp. 583 to 592. doi: 10.1016/0032-0633(65)90171-6.
- Clilverd, M. A., C. J. Rodger, T. Ulich, A. Seppälä, E. Turunen, A. Botman, and N. R. Thomson (2005), Modeling a large solar proton event in the southern polar atmosphere, *J. Geophys. Res.*, 110, A09307, doi: 10.1029/2004JA010922.

Coleman, T. F., and Y. Li (1996), An Interior, Trust Region Approach for Nonlinear Minimization Subject to Bounds. *SIAM Journal on Optimization*, 6, pp. 418-445, 1996, doi: 10.1137/0806023.

Collis, P. N., and M. T. Rietveld (1990), Mesospheric observations with the EISCAT UHF radar during polar cap absorption events: 1. Electron densities and negative ions, *Ann. Geophysicae*, Vol. 8, p.809-824.

Danskin, D. W., D. Boteler, E. Donovan, and E. Spanswick (2008), The Canadian riometer array. Proc. 12th International Ionospheric Effects Symposium (IES 2008), Alexandria, VA, USA, 13-15 May 2008, 80--86. Available online: <http://www.ntis.gov, PB2008112709>).

Davies, K. (1990), *Ionospheric Radio*, IEE Electromagnetic Series 31, Peter Peregrinus Ltd, London UK. ISBN 0 086341 186 X.

Dingle R. B., D. Arndt, and S. K. Roy (1957), The integrals  $\mathfrak{C}_p(x) = (p!)^{-1} \int_0^\infty \varepsilon^p (\varepsilon^2 + x^2 - 1e - \varepsilon d \varepsilon$  and  $\mathfrak{D}_p x = p! - 10^\infty \varepsilon p \varepsilon^2 + x^2 - 2e - \varepsilon d \varepsilon$  and their tabulation, *Appl. Sci. Res.*, 6(B), 155-164.

Dmitriev, A.V., P. T. Jayachandran, and L. -C. Tasi (2010), Elliptical model of cutoff boundaries for the solar energetic particles measured by POES satellites in December 2006, *J. Geophys. Res.* 115, A12244, doi:10.1029/2010JA015380.

Fisher, R. A. (1970), *Statistical Methods for Research Workers*, 14th Ed., Published by Edinburgh, Oliver and Boyd, ISBN 0050021702.

Foppiano, A. J., and P. A. Bradley (1983), Prediction of auroral absorption of high-frequency waves at oblique incidence, *Telecommunication J.*, Vol. 50, 547-560.

Friedrich, M., M. Harrich, K.M. Torkar and P. Stauning (2002), Quantitative Measurements with Wide-Beam Riometers, *J. Atmos. Solar Terr. Phys.* 64, pp. 359-365, 2002. doi: 10.1016/S1364-6826(01)00108-0.

Gledhill, J. A. (1986), The effective recombination coefficient of electrons in the ionosphere between 50 and 150 km, *Radio Sci.*, 21(3), 399–408, doi:10.1029/RS021i003p00399.

Hargreaves, J. K., H. Ranta, A. Ranta, E. Turunen, and T. Turunen (1987), Observations of the polar cap absorption event of February 1984 by the EISCAT incoherent scatter radar, *Planet. Space Sci.*, 35(7), 947-958, doi: 10.1016/0032-0633(87)90072-9.

Hargreaves, J. K., and M. J. Birch (2005), On the relations between proton influx and D-region electron densities during the polar-cap absorption event of 28–29 October 2003, *Annales Geophysicae*, 23, 3267–3276, doi: 10.5194/angeo-23-3267-2005.

Hargreaves, J. K., and D. L. Detrick (2002), Application of PCA events to the calibration of riometer systems, *Radio Sci.* 37, (3), 1035, 7-1 to 7-11, doi:10.1029/2001RS002465.

Hargreaves, J. K., A. V. Shirochkov, and A. D. Farmer (1993), The polar cap absorption event of 19-21 March 1990: recombination coefficients, the twilight transition and the midday recovery, *J. Atmos. Terr. Phys.*, 55(6), 857-862, doi: 10.1016/0021-9169(93)90026-U.

Honary, F., S. R. Marple, K. Barratt, P. Chapman, M. Grill, and E. Nielsen (2011), Digital Beam-forming Imaging Riometer Systems. *Review of Scientific Instruments*, 82 (3), 1-15, doi:10.1063/1.3567309.

Hunsucker, R. D., and J.K. Hargreaves (2003), *The high-latitude ionosphere and its effects on radio propagation*, Cambridge University Press, Cambridge, UK, ISBN 0 521 33083.

Ji, E.-Y., Y.-J. Moon, and J. Park (2014), Forecast of solar proton flux profiles for well-connected events, *J. Geophys. Res. Space Physics*, 119, 9383–9394, doi:10.1002/2014JA020333.

Kouznetsov, A., D. J. Knudsen, E. F. Donovan, and E. Spanswick (2014), Dynamics of the correlation between polar cap radio absorption and solar energetic proton fluxes in the interplanetary medium, *J. Geophys. Res.: Space Phys.* 119, doi: 10.1002/2013JA019024.

Kurt, V., A. Belov, H. Mavromichalaki, and M. Gerontidou (2004), Statistical analysis of solar proton events, *Annales Geophysicae* 22, 2255–2271, doi:10.5194/angeo-22-2255-2004.

Li, N., and J. Chen (2014), Asymmetry in diurnal variation of electron density in D region over Kunming, In General Assembly and Scientific Symposium (URSI GASS), 2014 XXXIth URSI, 1-4, 16-23 Aug. 2014, doi: 10.1109/URSIGASS.2014.6929739.

Little, C. G., and H. Leinbach (1959), The riometer - A device for the continuous measurement of ionospheric absorption, *Proc. IRE* 47(2), 315–320, doi:10.1109/JRPROC.1959.287299.

Neal, J. J., C. J. Rodger, and J. C. Green (2013), Empirical determination of solar proton access to the atmosphere: Impact on polar flight paths, *Space Weather*, 11, 420–433, doi: 10.1002/swe.20066.

Nesse Tyssøy, H., and J. Stadsnes (2015), Cutoff latitude variation during solar proton events: Causes and consequences, *J. Geophys. Res. Space Physics*, 120, 553–563, doi: 10.1002/2014JA020508.

Núñez, M. (2011), Predicting solar energetic proton events ( $E > 10$  MeV), *Space Weather*, 9, S07003, doi: 10.1029/2010SW000640.

Ondrášková, A, and A. A. Krivolutsky (2005), Solar cosmic rays and changes in the polar middle atmosphere and ionosphere, *J. Atmos. Solar-Terr. Phys.* 67(1–2), 211-218, doi: 10.1016/j.jastp.2004.07.033.

Ondrášková, A., A. A. Krivolutsky, and J. Laštovic (2003), Changes of the neutral and ionized composition in the D-region after solar proton event in October 1989 (model simulations), *Advances in Space Research*, 31(9), 2169-2176, doi: 10.1016/S0273-1177(03)00130-3.

Ondrášková, A., A. A. Krivolutsky, A. Kukoleva, T. Vyushkova, A. Kuminov and G. Zakharov (2008), Response of the lower ionosphere to solar proton event on July 14, 2000. Model simulations over both poles, *J. Atmos. and Solar-Terr. Phys.*, 70, 539-545, doi: 10.1016/j.jastp.2007.08.060.

Osepian, A., V. Tereschenko, P. Dalin, and S. Kirkwood (2008), The role of atomic oxygen concentration in the ionization balance of the lower ionosphere during solar proton events, *Ann. Geophys.*, 26, 131-143, doi:10.5194/angeo-26-131-2008.

Osepian, A., S. Kirkwood, P. Dalin, and V. Tereschenko (2009), D-region electron density and effective recombination coefficients during twilight – experimental data and modelling during solar proton events, *Ann. Geophys.*, 27, 3713-3724, doi:10.5194/angeo-27-3713-2009.

Patterson, J. D., T. P. Armstrong, C. M. Laird, D. L. Detrick and A. T. Weatherwax (2001), Correlation of solar energetic protons and polar cap absorption, *J. Geophys. Res.*, 106(A1), 109-163, doi: 10.1029/2000JA002006.

Picone, J. M., A. E. Hedin, D. P. Drob and A. C. Aikin (2002), NRLMSISE-00 empirical model of the atmosphere: Statistical comparisons and scientific issues, *J. Geophys. Res.* 107(A12), 1468, doi: 10.1029/2002JA009430.

Potemra, T.A. (1972), The empirical connection of riometer absorption to solar protons during PCA events, *Radio Sci.*, 7(5), 571-577, doi: 10.1029/RS007i005p00571.

Potemra, T.A., and A. J. Zmuda (1972), Solar electrons and alpha particles during Polar-Cap Absorption events, *J. Geophys. Res.* 77(34), 6916-6921, doi: 10.1029/JA077i034p06916.

Ranta, H., H. Yamagishi, and P. Stauning (1995), Twilight anomaly, midday recovery and cutoff latitudes during the intense polar cap absorption event of March 1991, *Ann. Geophys.*, 13, 262-276, doi: 10.1007/s00585-995-0262-1.

Reagan, J.B., and T.M. Watt (1976), Simultaneous satellite and radar studies of the D region ionosphere during the intense solar particle events of August 1972, *J. Geophys. Res.*, 81(25), 4579-4596.,doi: 10.1029/JA081i025p04579.

Rogers, N. C., and F. Honary (2015), Assimilation of Real-time Riometer Measurements into Models of 30 MHz Polar Cap Absorption, *J. Space Weather Space Clim.*, 5(A8), doi: 10.1051/swsc/2015009.

Rosenberg, T. J., D. L. Detrick, D. Venkatesan and G. van Bavel (1991), A comparative study of imaging and broad-beam riometer measurements: The effect of spatial structure on the frequency dependence of auroral absorption, *J. Geophys. Res.*, 96(A10), 17793–17803, doi: 10.1029/91JA01827.

Rostoker, G., J. C. Samson, F. Creutzberg, T. J. Hughes, D. R. McDiarmid, A. G. McNamara, A. Vallance Jones, D. D. Wallis and L. L. Cogger (1995), CANOPUS – A ground-based instrument array for remote sensing the high latitude ionosphere during the ISTP/GGS program, *Space Science Reviews*, 71, 743-760. doi: 10.1007/BF00751349.

Sauer, H. H. (1968), Nonconjugate aspects of recent polar cap absorption events, *J. Geophys. Res.* 73(9), 3058-3062, doi: 10.1029/JA073i009p03058

- Sauer, H. H., and D. C. Wilkinson (2008), Global mapping of ionospheric HF/VHF radio wave absorption due to solar energetic protons, *Space Weather*, 6, S12002. doi: 10.1029/2008SW000399.
- Schumer, E.A. (2009), Improved modeling of midlatitude D-region ionospheric absorption of high frequency radio signals during solar x-ray flares, Ph.D. Dissertation, AFIT/DS/ENP/09-J01, United States Air Force, Wright-Patterson Air Force Base, Ohio, USA. Available online: [www.dtic.mil/dtic/tr/fulltext/u2/a516063.pdf](http://www.dtic.mil/dtic/tr/fulltext/u2/a516063.pdf).
- Sellers, B., F. A. Hanser, M. A. Stroschio, and G. K. Yates (1977), The night and day relationships between polar cap riometer absorption and solar protons, *Radio Sci.*, 12, 779-789, doi: 10.1029/RS012i005p00779.
- Shea, M. A., and D.F. Smart (1990), A summary of major solar proton events, *Solar Phys.*, 127, 297-320, doi: 10.1007/BF00152170.
- Smart, D. F., M. A. Shea, E. O. Fluckiger, A. J. Tylka, and P. R. Boberg (1999), Changes of calculated vertical cutoff rigidities at the altitude of the International Space Station as a function of geomagnetic activity, *Proc. Int. Cosmic Ray Conf.*, 7, 337- 340.
- Stauning, P. (1996), High-latitude D- and E-region investigations using imaging riometer observations, *J. Atmos. Terr. Phys.*, 58(6), 765-783, doi:10.1016/0021-9169(95)00073-9.
- Størmer, C. (1955), *The Polar Aurora*, Clarendon Press, Oxford.
- Swider, W. (1977), Aeronomic aspects of the polar D-region, *Space Sci. Rev.*, 20, 69-114. doi: 10.1007/BF02186894.
- Temerin, M., and X. Li (2002), A new model for the prediction of Dst on the basis of the solar wind, *J. Geophys. Res.*, 107(A12), 1472, doi:10.1029/2001JA007532.

Temerin, M., and X. Li (2006), Dst model for 1995–2002, *J. Geophys. Res.*, 111, A04221, doi: 10.1029/2005JA011257.

Verronen, P. T., A. Seppälä, M. A. Clilverd, C. J. Rodger, E. Kyrölä, C. -F. Enell, T. Ulich, and E. Turunen (2005), Diurnal variation of ozone depletion during the October–November 2003 solar proton events, *J. Geophys. Res.*, 110, A09S32, doi: 10.1029/2004JA010932.

Verronen, P. T., T. Ulich, E. Turunen, and C. J. Rodger (2006), Sunset transition of negative charge in the D-region ionosphere during high-ionization conditions, *Ann. Geophys.*, 24, 187–202, doi: 10.5194/angeo-24-187-2006.

Verronen, P. T., M. E. Andersson, A. Kero, C.-F. Enell, J. M. Wissing, E. R. Talaat, K. Kauristie, M. Palmroth, T. E. Sarris, and E. Armandillo (2015), Contribution of proton and electron precipitation to the observed electron concentration in October–November 2003 and September 2005, *Ann. Geophys.*, 33, 381–394, doi: 10.5194/angeo-33-381-2015.

Vickrey, J. F., R. R. Vondrak, and S. J. Matthews (1982), Energy deposition by precipitating particles and Joule dissipation in the auroral ionosphere, *J. Geophys. Res.*, 87, 5184, doi: 10.1029/JA087iA07p05184.

Warrington, E. M., A. J. Stocker, D.R. Siddle, J. Hallam, H. A. H. Al-Behadili, N. Y. Zaalov, F. Honary, N. C. Rogers, D.H. Boteler, and D.W. Danskin (2016a), Near real-time input to an HF propagation model for nowcasting of HF communications with aircraft on polar routes, *Radio Sci.*, 51, 1048–1059, doi: 10.1002/2015RS005880.

Accepted Article

Warrington, E. M., N. C. Rogers, A. J. Stocker, J. Hallam, D. R. Siddle, H. A. H. Al-  
Behadili, N. Zaalov, F. Honary, D. Boteler, and D. Danskin (2016b), Progress  
towards a propagation prediction service for HF communications with aircraft on  
trans-polar routes. Proc. Nordic HF conference, Fårö, Gotland, 15-17 August 2016,  
Available online: <http://hdl.handle.net/2381/37759>.

Wing, S., J. R. Johnson, J. Jen, C.-I. Meng, D. G. Sibeck, K. Bechtold, J. Freeman, K.  
Costello, M. Balikhin, and K. Takahashi (2005), Kp forecast models, J. Geophys.  
Res., 110, A04203, doi: 10.1029/2004JA010500.

Zmuda, A. J., and T. A. Potemra (1973), HF absorption near the polar cap edge during PCA  
events, J. Geophys. Res., 78(25), 5818-5821, doi: 10.1029/JA078i025p05818.

Table 1. Riometer locations and operating frequencies.

Riometer	Code	Geodetic latitude (°N)	Geodetic longitude (°E)	Frequency (MHz)
<b>NORSTAR riometers, Canada</b>				
Contwoyto Lake	cont	65.75	-111.26	30.0
Dawson	daws	64.05	-139.11	30.0
Eskimo Point	eski	61.11	-94.05	30.0
Fort Churchill	fchu	58.76	-94.08	30.0
Fort Simpson	fsim	61.76	-121.23	30.0
Fort Smith	fsmi	60.03	-111.95	30.0
Gillam	gill	56.38	-94.64	30.0
Island Lake	isll	53.86	-94.66	30.0
Fort McMurray	mcmu	56.65	-111.21	30.0
Pinawa	pina	50.20	-96.04	30.0
Rabbit Lake	rabb	58.23	-103.68	30.0
Rankin Inlet	rank	62.82	-92.11	30.0
Taloyoak	talo	69.54	-93.55	30.0
<b>Lancaster University riometer (operated by SGO)</b>				
Kilpisjärvi, Finland (IRIS)	kil	69.05	20.79	38.2

<b>SGO riometers</b>				
Abisko, Sweden	abi	68.36	18.82	30.0
Hornsund, Svalbard	hor	77.00	15.60	30.0
Jyväskylä, Finland	jyv	62.42	25.28	32.4
Oulu, Finland	oul	65.09	25.89	30.0
Rovaniemi, Finland	rov	66.78	25.94	32.4
Sodankylä, Finland	sod	67.42	26.39	30.0
<b>NRCan riometers, Canada</b>				
Alert	ale	82.52	-62.27	30.0
Cambridge Bay	cbb	69.10	-105.00	30.0
Inuvik	inu	68.41	-133.77	30.0
Iqaluit	iqu	63.70	-68.50	30.0
Meanook	mea	54.60	-113.30	30.0
Ottawa	ott	45.40	-75.50	30.0
Pond Inlet	pon	72.68	-77.95	30.0
Saskatoon	sas	52.16	-106.53	30.0
Sanikiluaq	snk	56.30	-79.00	30.0
St. John's	stj	47.60	-52.70	30.0
Yellowknife	yck	62.50	-114.50	30.0

Table 2. Start and end times of 13 SPEs.

<b>Start time (UT)</b>	<b>End time (UT)</b>
20/04/98 14:00	24/04/98 17:45
14/07/00 10:45	19/07/00 23:30
08/11/00 23:50	13/11/00 07:45
02/04/01 23:40	06/04/01 22:55
15/04/01 14:10	17/04/01 19:50
24/09/01 12:15	30/09/01 17:10
01/10/01 11:45	05/10/01 04:45
04/11/01 17:05	10/11/01 07:15
22/11/01 23:20	27/11/01 16:55
26/12/01 06:05	28/12/01 10:40
21/04/02 02:25	26/04/02 07:15
16/01/05 02:10	22/01/05 18:00
08/09/05 02:15	13/09/05 01:15

Table 3. Optimum parameters  $E_t$  and  $m$  with associated (minimized) RMS error for Model A (Eqn. (3)) and RMS errors for DRAP and Model B (Equation (9), based on 13 SPEs 1995-2010 for four polar-cap riometers (individually and combined).

	Model A (Threshold model)			DRAP	Model B (Multi-channel model)	
Riometer	Optimal $E_t$ (MeV)	$m(E_t)$ (dB p $fu^{-0.5}$ )	RMSE (dB)	RMSE (dB)	RMSE (dB)	Number of measurements (5-min. medians)
Day ( $\chi < 60^\circ$ )						
cont	7.18	0.092	0.738	1.240	0.629	777
eski	8.65	0.122	0.740	0.784	0.730	1249
rank	7.90	0.104	0.815	1.090	0.800	962
talo	2.74	0.063	0.977	1.883	0.974	818
All four riometers	6.27	0.095	0.984	1.256	0.973	3806
Night ( $\chi > 120^\circ$ )						
cont	1.19	0.011	0.200	0.485	0.201	1195
eski	1.39	0.015	0.269	0.369	0.260	748
rank	2.22	0.013	0.236	0.404	0.237	1383
talo	2.05	0.012	0.292	0.531	0.284	1203
All four riometers	1.75	0.013	0.271	0.458	0.271	4529

Table 4. Allowed parameter ranges and optimized values (Mean  $\pm$  SD) of best-fit parameters presented in Figure 5 for the twilight model of Equation (14) with  $E_t = 5$  MeV.

Parameter	Limits of optimization			Optimum values	
	Initial estimate	Lower limit	Upper limit	Sunrise ( $0 \leq LT < 12$ )	Sunset ( $12 \leq LT < 24$ )
$m_n$ (dB pfu <sup>-0.5</sup> )	0.02	0.002	0.2	0.0196 $\pm$ 0.0109	0.0225 $\pm$ 0.00829
$m_d$ (dB pfu <sup>-0.5</sup> )	0.115	0.0115	1.15	0.101 $\pm$ 0.0218	0.106 $\pm$ 0.0182
$\chi_l$ (°)	80	50	90	73.8 $\pm$ 7.21	82.6 $\pm$ 4.57
$\chi_u$ (°)	100	90	120	97.9 $\pm$ 2.42	100.6 $\pm$ 2.44

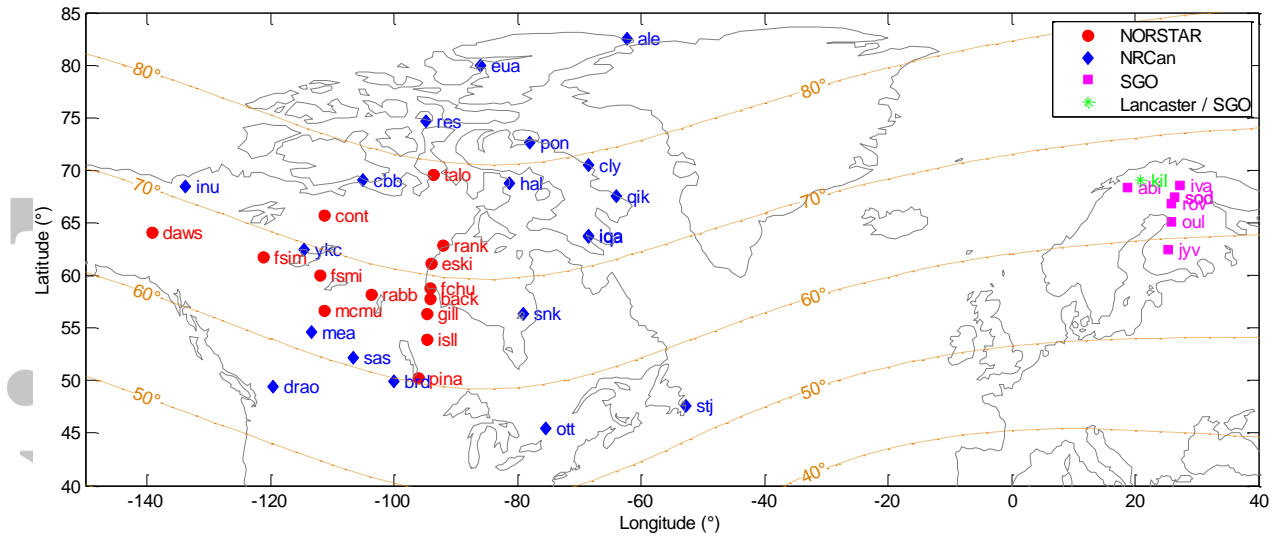


Figure 1. Locations of riometers in the Global Riometer Array (GloRiA), labeled by operating institution. Corrected geomagnetic latitude contours are shown for the year 2001 at 50 km altitude.

Accepted

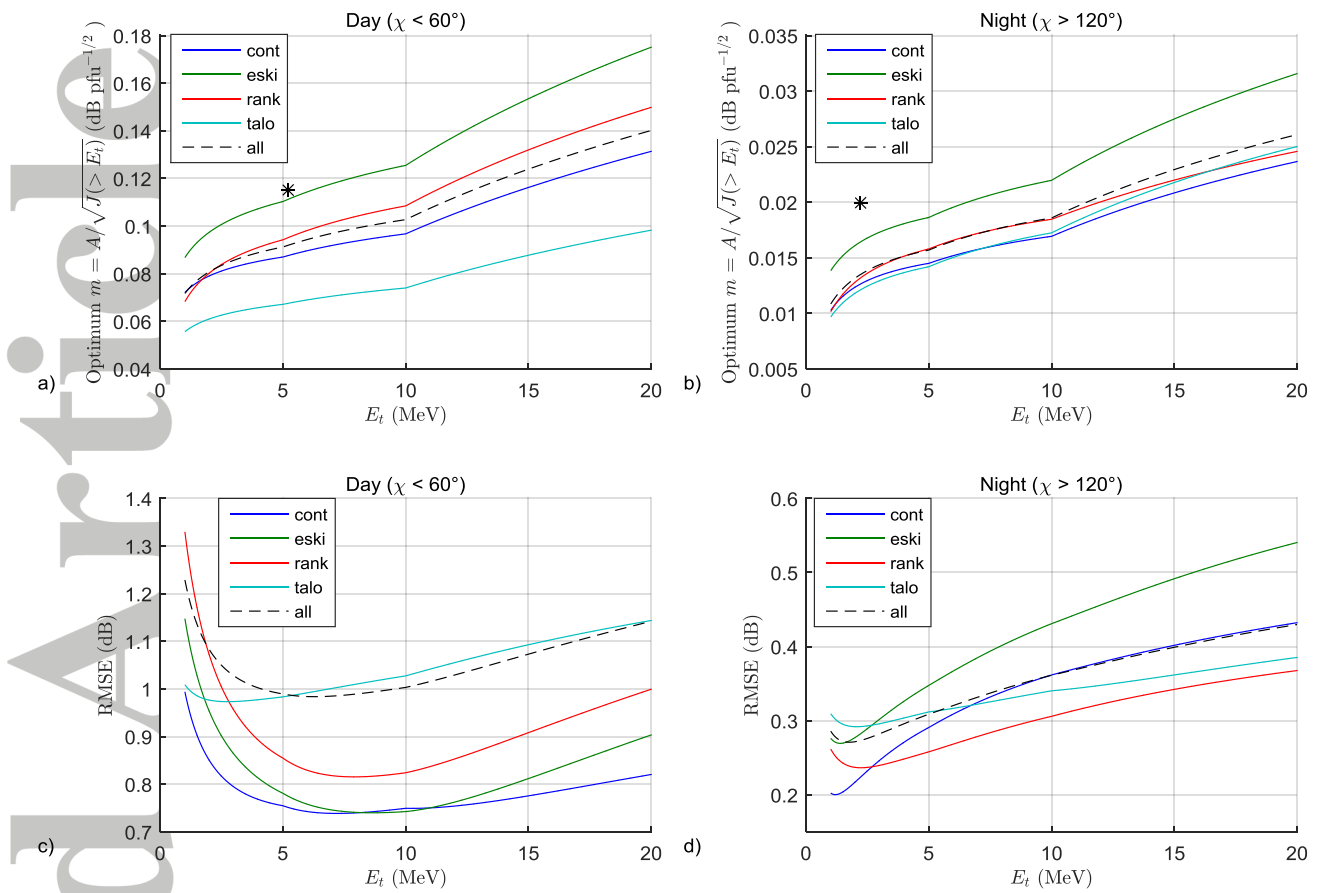


Figure 2. Optimal  $m$  for a range of  $E_t$  for four polar-cap riometers (individually and combined) for 13 SPEs: a) Day ( $\chi < 60^\circ$ ); b) Night ( $\chi > 120^\circ$ ). Asterisks (\*) indicate DRAP model values. The associated optimal RMSE values are shown for c) Day and d) Night.

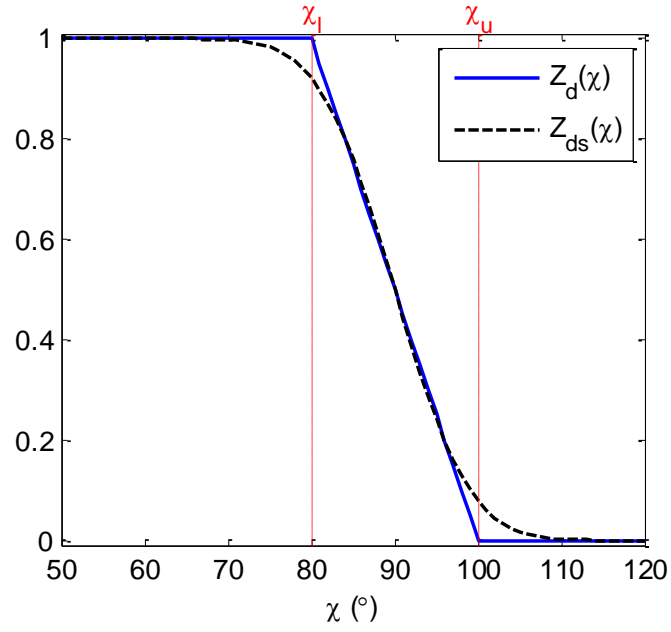


Figure 3. The weighting function,  $Z_d(\chi)$  (Equation (8)), as parameterized in the DRAP model, and an alternative smooth function  $Z_{ds}(\chi)$  (Equation (12)).

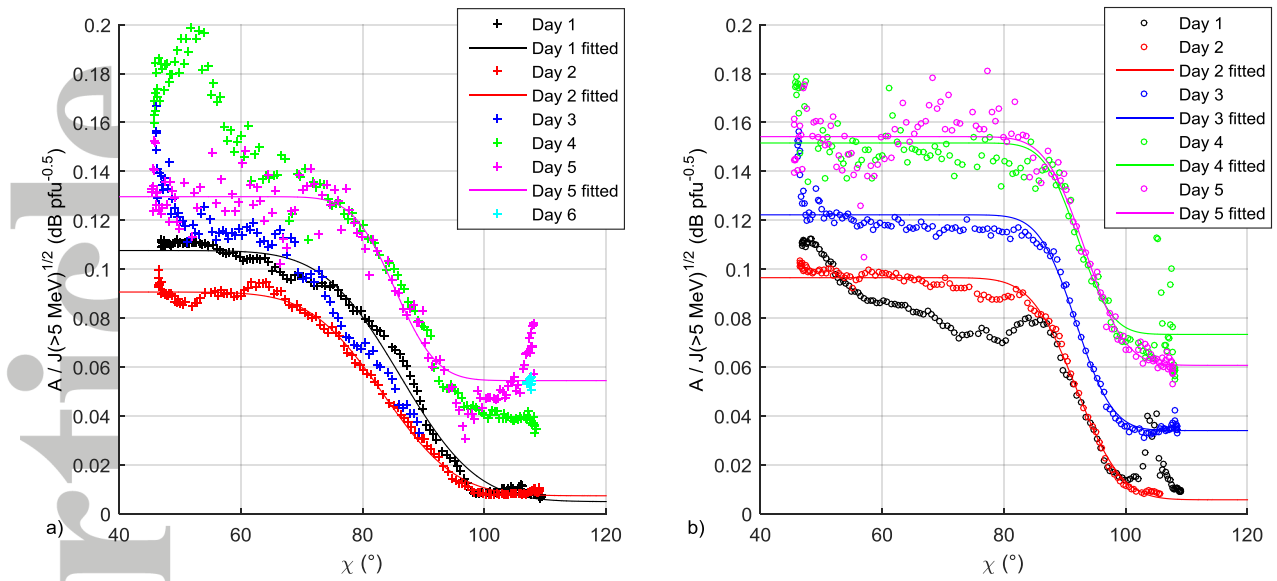


Figure 4. Ratio of absorption (dB) at the Fort Churchill riometer to the square root of  $> 5$  MeV proton flux for the SPE commencing 21 April 2002 as a function of solar-zenith angle. a) sunrise (0-12 Local Time), b) sunset (12-24 LT). Solid lines represent best fit to the model (Equation (14)).

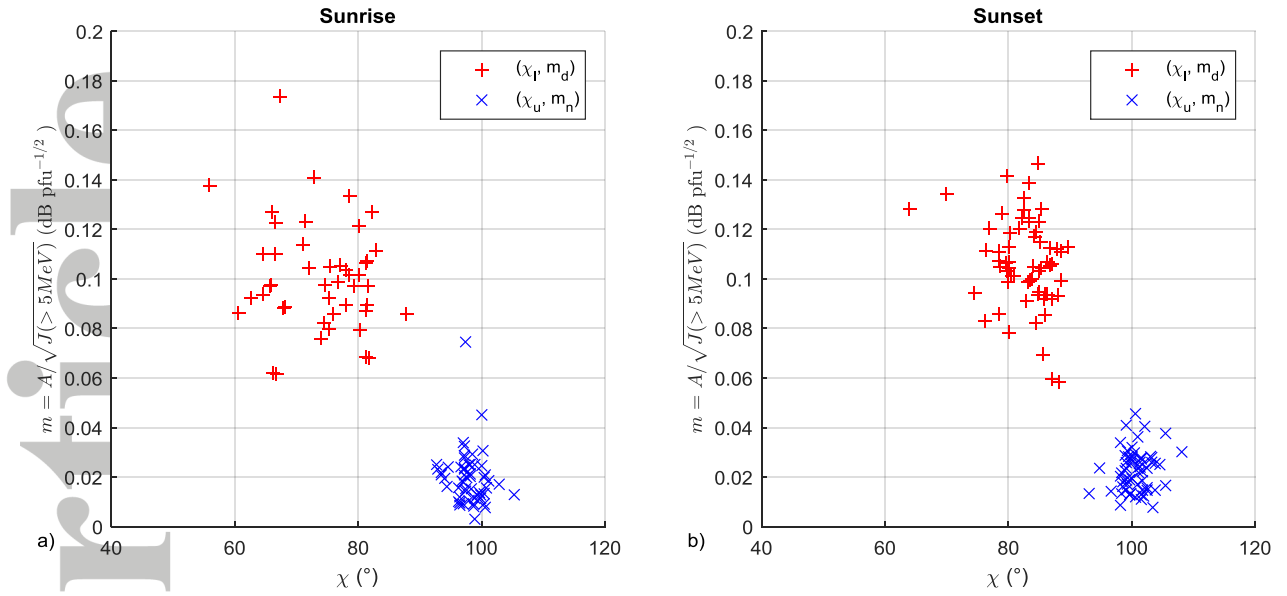


Figure 5. Optimal parameter pairs  $(\chi_l, m_d)$  (red '+') and  $(\chi_u, m_n)$  (blue 'x') minimising the mean-squared error between Equation (14) and  $m_5(\chi)$  measurements at four polar-cap riometers (talo, cont, rank, eski) for 13 SPEs. a) Sunrise ( $0 \leq \text{LT} < 12$ ); b) Sunset ( $12 \leq \text{LT} < 24$ ).

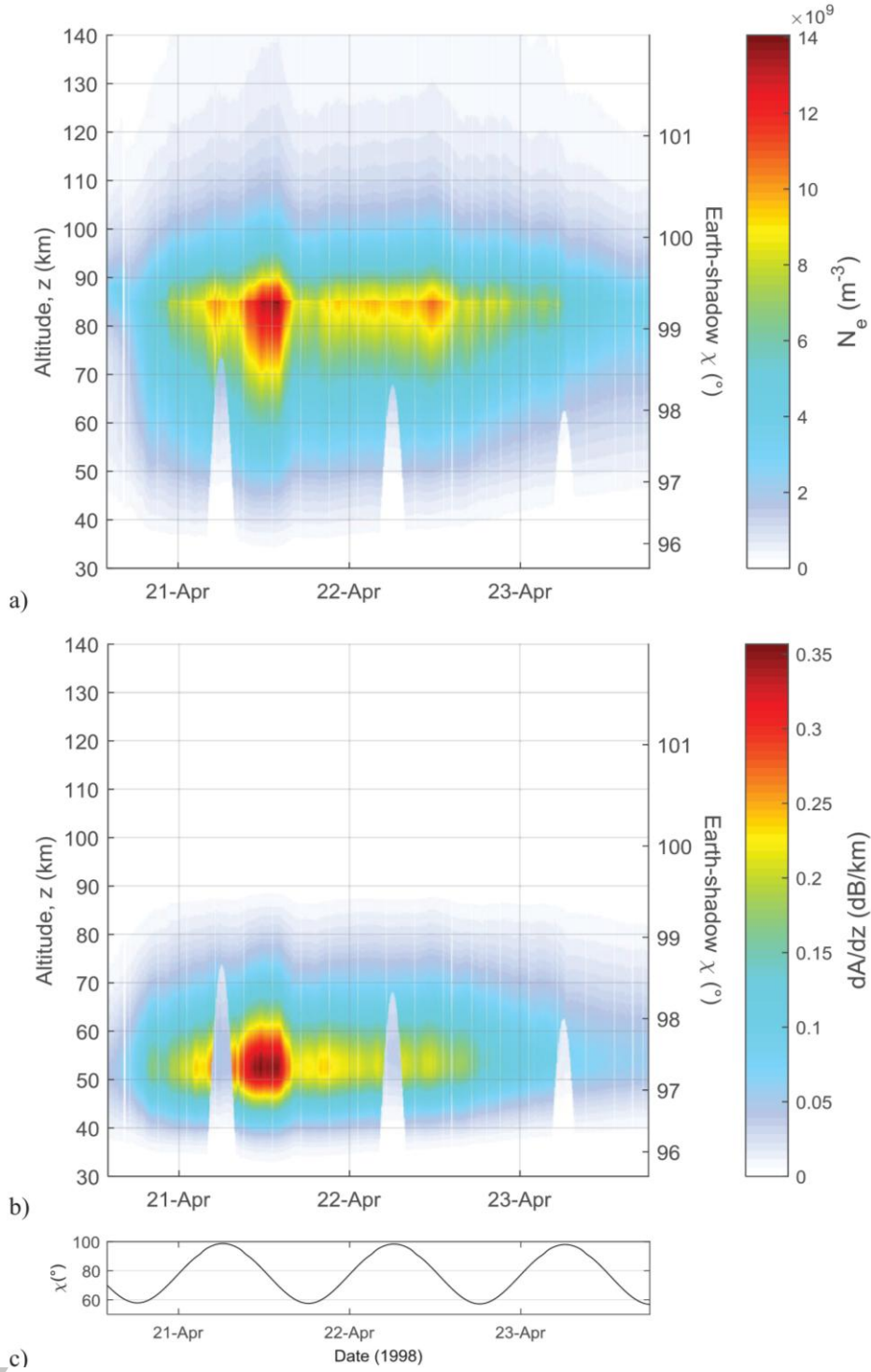


Figure 6. Predictions of a)  $N_e(t, z)$  and b)  $\partial A/\partial z$  at 30 MHz for the April 1998 SPE at the Taloyoak riometer using the model of *Rogers and Honary* [2015] with  $h_{Dd} = 5.77$  km  $h_{Dn} = 2.11$  km (optimum for this SPE/riometer). (Times corresponding to missing or invalid riometer data are not plotted). The right axes indicate the zenith angle of the Earth shadow line. c) Solar-zenith angle,  $\chi$ .

Accepted Article

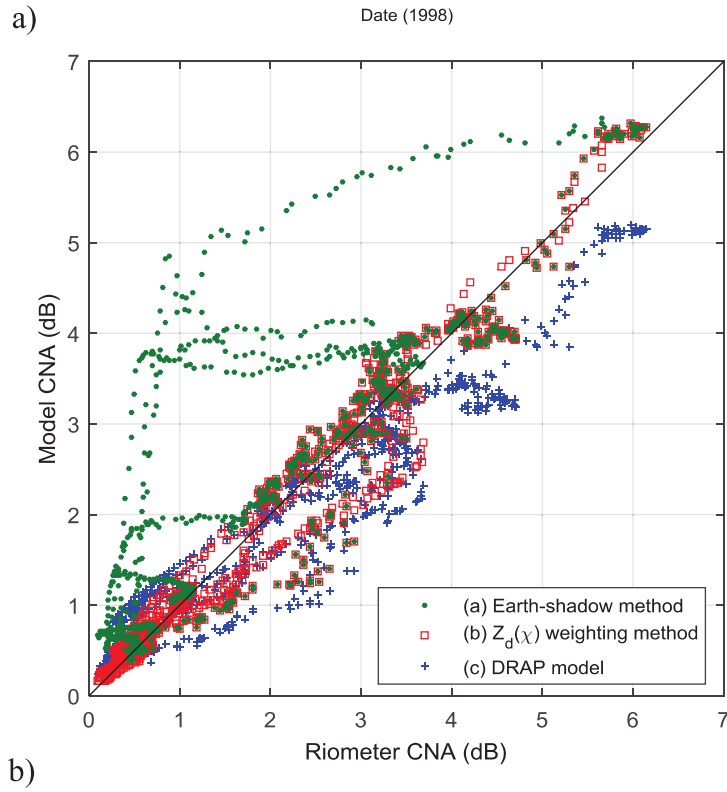
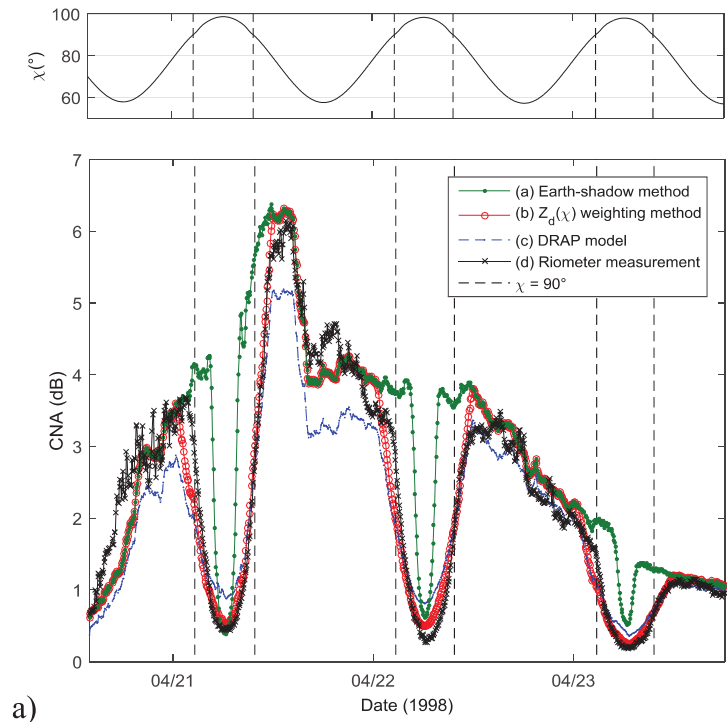


Figure 7. Measured and modeled 30 MHz CNA at the Taloyoak riometer for the SPE of April 1998. a) CNA vs. time (with  $\chi$  shown at top); b) model CNA vs. measurements (5-minute medians): Model (a) is *Rogers and Honary, [2015]* full-profile model (with Earth shadow transition), with  $h_{Dd} = 5.77$  km  $h_{Dn} = 2.11$  km (optimum for this event/riometer); model (b) is as (a) but substituting Earth-shadow transition with the  $Z_d(\chi)$  weighting from DRAP; (c) DRAP model; (d) riometer measurements.

Accepted Article

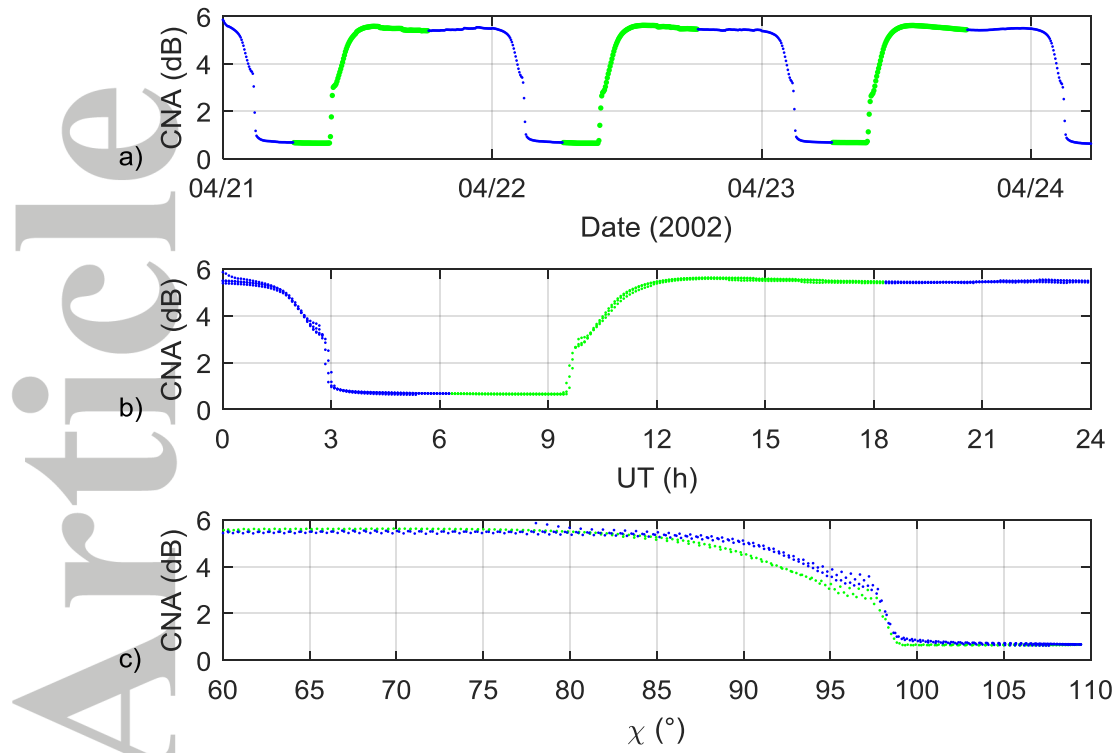


Figure 8. SIC model estimates of CNA at the Fort Churchill riometer for April 2002. Green points represent 0-12 LT (sunrise), blue represents 12-24 LT (sunset). A constant proton flux is modeled. a) CNA vs. date. b) CNA vs. UT, c) CNA vs.  $\chi$ .

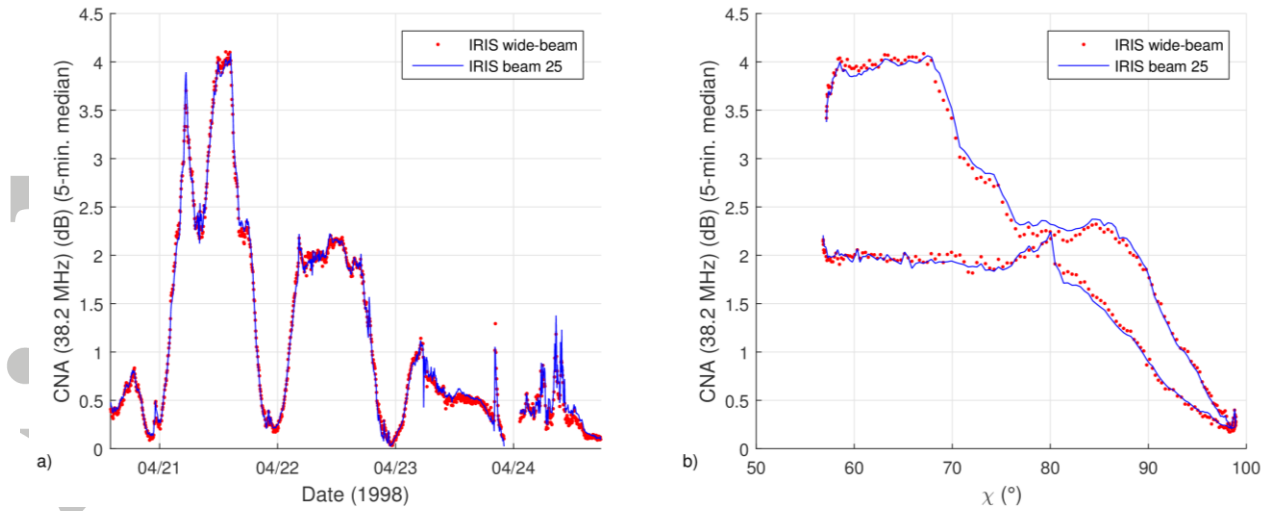


Figure 9. Comparison of 38.2 MHz CNA on the wide-beam and the central narrow beam (beam 25) of the IRIS imaging riometer in Kilpisjärvi during a SPE. a) CNA vs time. b) CNA vs zenith angle (local noon (10:37 UT) 21-22 April 1998 only).

Accepted

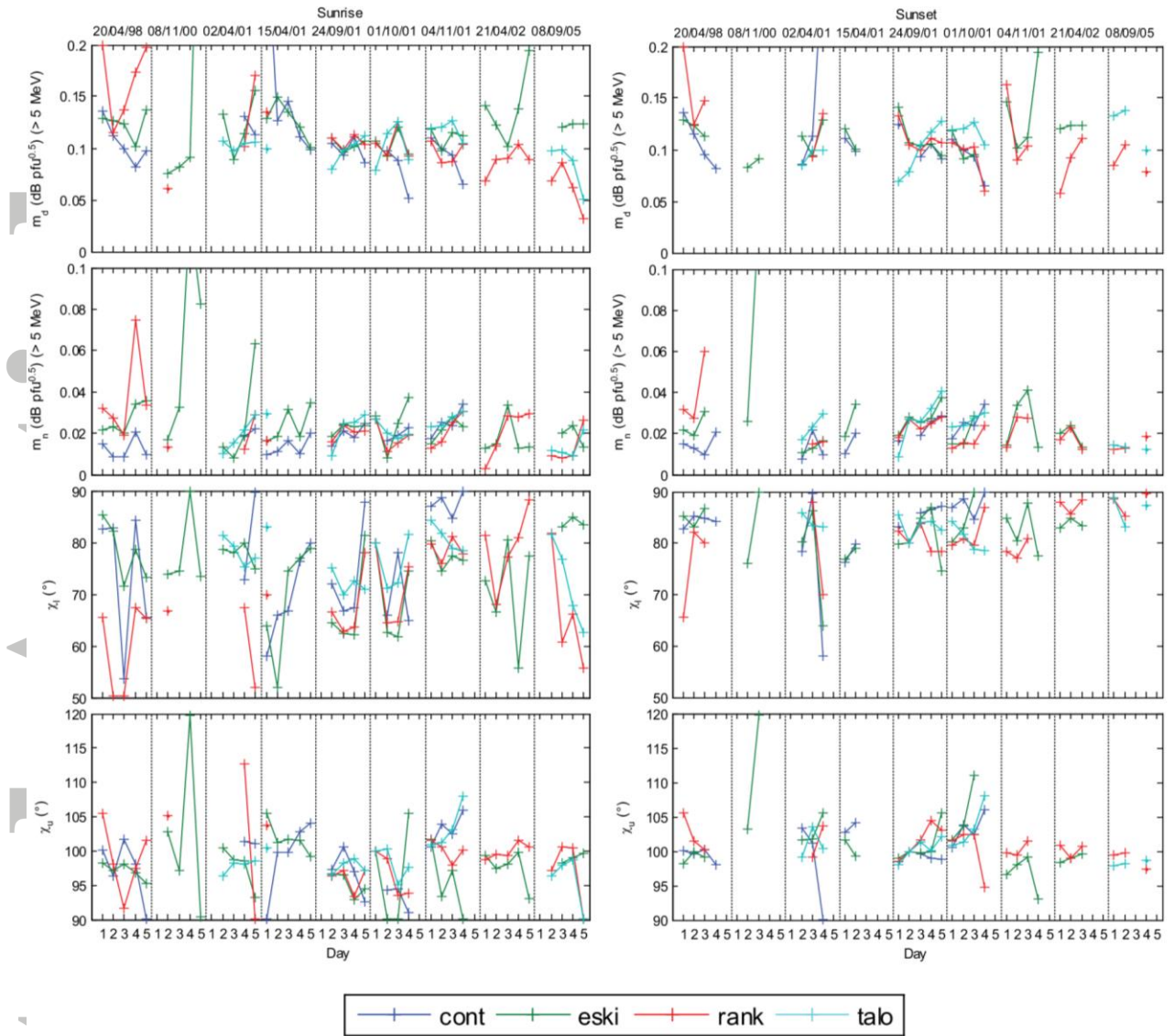


Figure 10. Best-fit model parameters (Eqn (14)) for the first 5 days of each of 9 SPEs. Each colored line represents a separate riometer. Left: Sunrise (00-12 LT); Right: Sunset (12-24 LT).

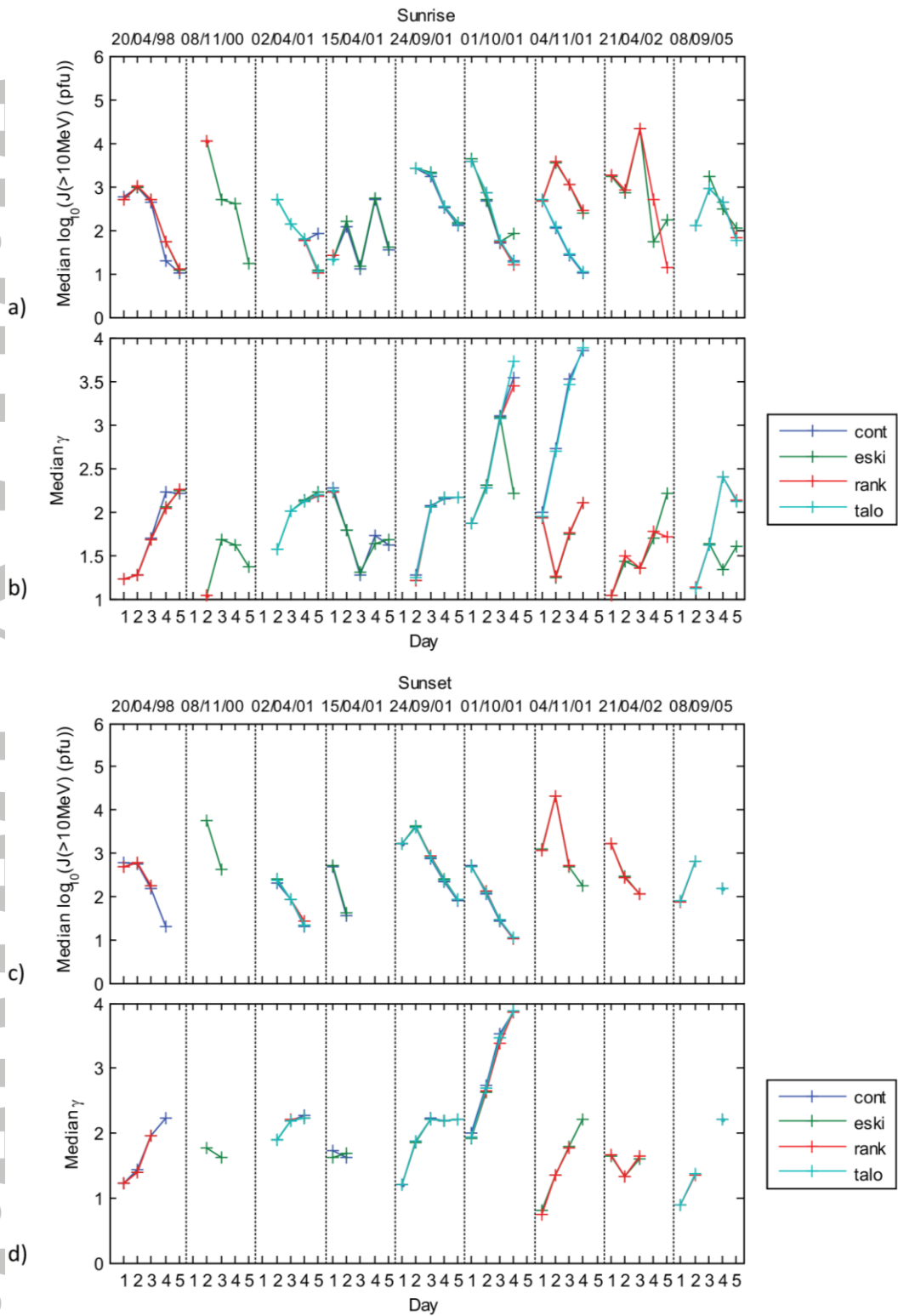


Figure 11. Median values of a) integral flux  $J(>10\text{ MeV})$  (0-12 LT), b) spectral index ( $\gamma_{(10-30\text{MeV})}$ ) (0-12 LT), c) integral flux  $J(>10\text{ MeV})$  (12-24 LT) and d) spectral index ( $\gamma_{(10-30\text{MeV})}$ ) (12-24 LT).

# ACCEPTED MANUSCRIPT

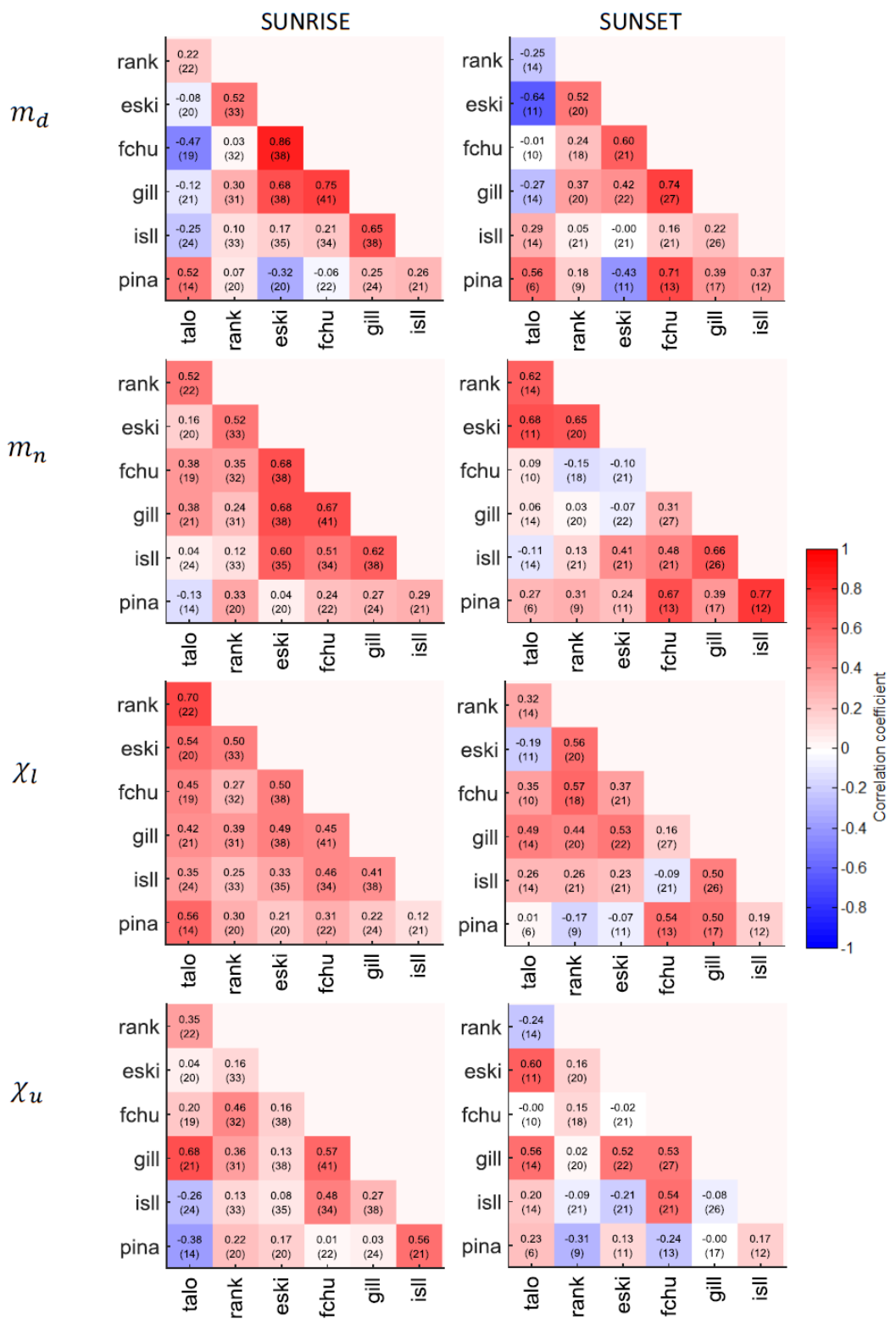
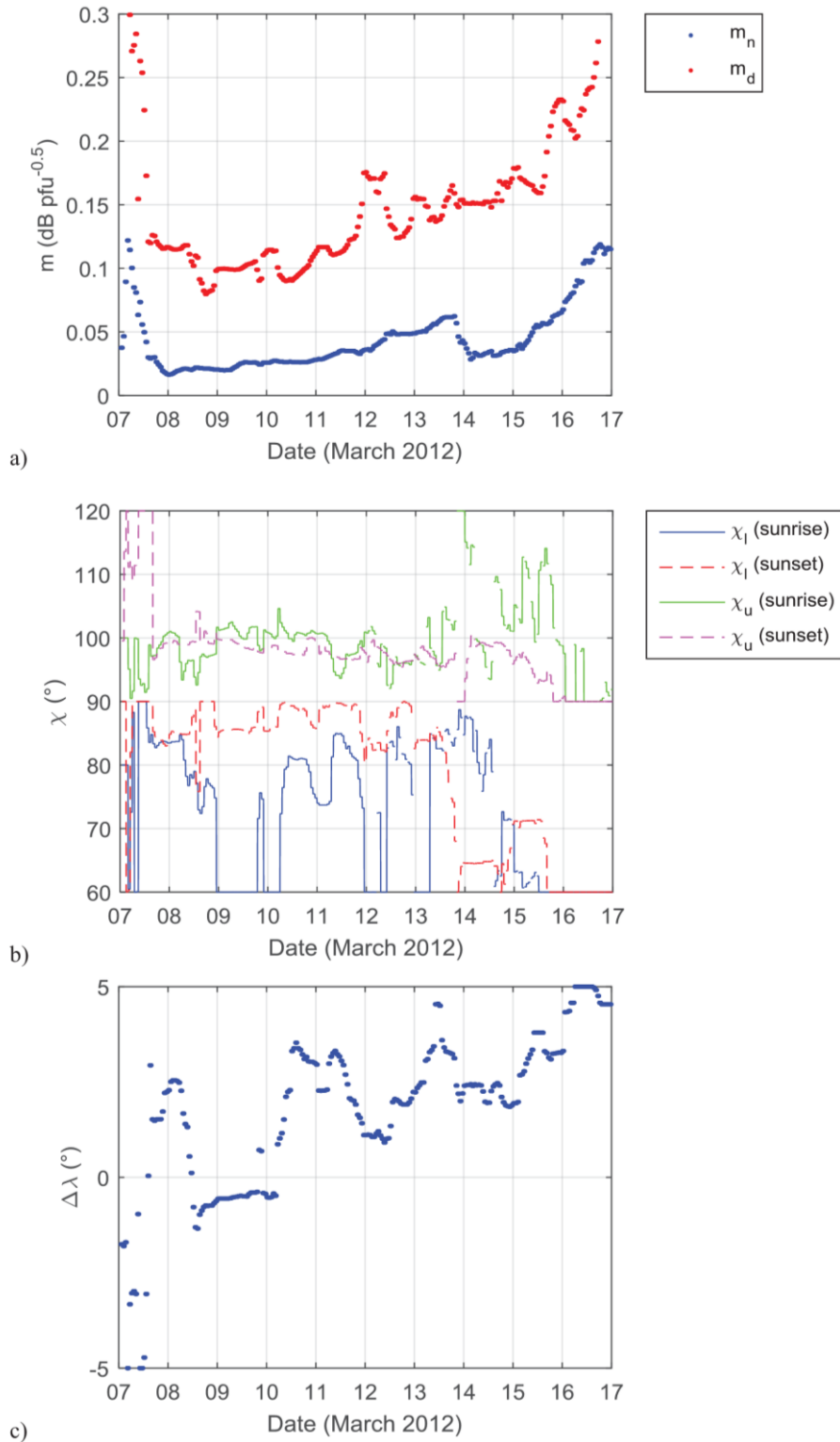


Figure 12. Correlation coefficients for a)  $m_d$ , b)  $m_n$ , c)  $\chi_l$  and d)  $\chi_u$  fitted using the 3-line model at sunrise (left panels) and sunset (right panels) between pairs of riometers in the Churchill line. Numbers in brackets indicate the number of data points used in each correlation.



**Figure 13.** Empirical twilight model parameters optimized in real time from 25 riometers during a SPE on 7-16 March 2012. a)  $m_n$  and  $m_d$ , b)  $\chi_l$  and  $\chi_u$  (sunrise and sunset), c)  $\Delta\lambda$  (equatorial shift in rigidity cutoff).

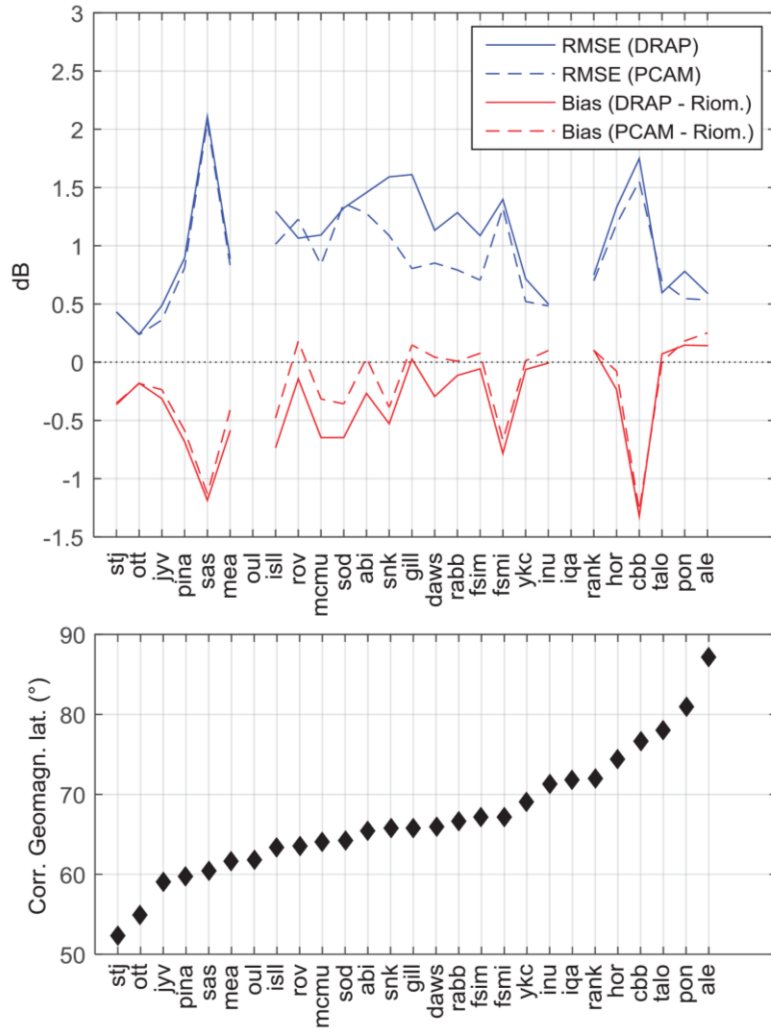


Figure 14. a) RMSE and bias (mean error) at each riometer for the DRAP model and the real-time optimized model (PCAM). b) Corrected geomagnetic latitudes of each riometer.